



This is a repository copy of *An IRAK1-PIN1 signalling axis drives intrinsic tumour resistance to radiation therapy*.

White Rose Research Online URL for this paper:
<http://eprints.whiterose.ac.uk/145319/>

Version: Accepted Version

Article:

Liu, P.H. orcid.org/0000-0001-5037-085X, Shah, R.B., Li, Y. et al. (20 more authors) (2019) An IRAK1-PIN1 signalling axis drives intrinsic tumour resistance to radiation therapy. *Nature Cell Biology*, 21 (2). pp. 203-213. ISSN 1465-7392

<https://doi.org/10.1038/s41556-018-0260-7>

Reuse

Items deposited in White Rose Research Online are protected by copyright, with all rights reserved unless indicated otherwise. They may be downloaded and/or printed for private study, or other acts as permitted by national copyright laws. The publisher or other rights holders may allow further reproduction and re-use of the full text version. This is indicated by the licence information on the White Rose Research Online record for the item.

Takedown

If you consider content in White Rose Research Online to be in breach of UK law, please notify us by emailing eprints@whiterose.ac.uk including the URL of the record and the reason for the withdrawal request.



eprints@whiterose.ac.uk
<https://eprints.whiterose.ac.uk/>



Published in final edited form as:

Nat Cell Biol. 2019 February ; 21(2): 203–213. doi:10.1038/s41556-018-0260-7.

An IRAK1-PIN1 Signalling Axis Drives Intrinsic Tumour Resistance to Radiation Therapy

Peter H. Liu^{1,2}, Richa B. Shah^{1,2}, Yuanyuan Li^{1,2}, Arshi Arora³, Peter Man-Un Ung⁴, Renuka Raman^{1,2}, Andrej Gorbatenko⁵, Shingo Kozono⁶, Xiao Zhen Zhou⁶, Vincent Brechin^{1,2,†}, John M. Barbaro^{1,2,‡}, Ruth Thompson^{1,2,§}, Richard M. White⁷, Julio A Aguirre-Ghiso¹, John V. Heymach⁸, Kun Ping Lu⁶, Jose M. Silva⁵, Katherine S. Panageas³, Avner Schlessinger⁴, Robert G. Maki^{1,2,¶}, Heath D. Skinner⁸, Elisa de Stanchina⁹, and Samuel Sidi^{1,2,*}

¹Department of Medicine, Division of Hematology and Medical Oncology, Tisch Cancer Institute, Icahn School of Medicine at Mount Sinai, New York, NY, USA.

²Department of Cell, Developmental and Regenerative Biology, The Graduate School of Biomedical Sciences, Icahn School of Medicine at Mount Sinai, New York, NY, USA.

³Department of Epidemiology and Biostatistics, Memorial Sloan Kettering Cancer Center, New York, NY, USA.

⁴Department of Pharmacological Sciences, Icahn School of Medicine at Mount Sinai, New York, NY, USA.

Users may view, print, copy, and download text and data-mine the content in such documents, for the purposes of academic research, subject always to the full Conditions of use:http://www.nature.com/authors/editorial_policies/license.html#terms

*Correspondence to: samuel.sidi@mssm.edu.

Author Contributions:

P.H.L. performed the zebrafish drug screen with the assistance of J.M.B and V.B.; all zebrafish experiments with the exception of TUNEL and caspase-3 assays (V.B.) and p53atgMO, myd88MO, and hIRAK1 WT, K/R and E3A rescue assays (Y.L); and SEA analyses under the supervision of A.S. and S.S. R.B.S performed all cell culture assays with the assistance of P.H.L. and R.T. and analyzed the data with P.H.L, Y.L., and S.S. R.G.M. purchased the radioresistant cell lines and assisted with translational analyses. E.d.S., R.M.W. and S.S. conceived the xenograft study, which was performed by E.d.S. and analyzed by R.R. A.A. performed TCGA analyses under the supervision of K.S.P. and analyzed the data with R.M.W. and S.S. P.M.U.U. performed docking studies under the supervision of A.S. A.G. generated the IRAK1 KO under the supervision of J.M.S. S.K. and X.Z.Z. performed in vitro isomerase assays under the supervision of K.P.L. H.D.S. analyzed PIN1 expression levels in the MDACC HNSCC cohort with J.V.H' s assistance. S.S. conceived the study, supervised the project and wrote the paper.

Competing interests:

The authors declare no competing interests.

Additional information

Supplementary information is available for this paper at

Reprints and permissions information is available at www.nature.com/reprints.

Correspondence and requests for materials should be addressed to S.S.

Code Availability

All codes used are referenced in the Methods sections hereabove.

Data Availability

Whole-genome expression array data that support the findings of this study have been deposited in the Gene Expression Omnibus (GEO) under accession code GSE67614. The human HNSCC and BRCA data were derived from the TCGA Research Network: <http://cancergenome.nih.gov/>. The data-set derived from this resource that supports the findings of this study is available in Supplemental Table 4 (see sheet S3). Source data for Figs. 1e, 2b,d, 3c,e-f, 4a-e,g-h,m-n, 5b,d, 6c-j, 7a-d,f-g and Supplementary Figs. 1b, 2a-b, 3, 4a-f,k-l, 5, 6c-n, and 7c-d have been provided as Supplementary Table 4. The full image dataset that supports the findings in Figs. 3e-f has been deposited in Figshare under accession code 10.6084/m9.figshare.7427942. All other data supporting the findings of this study are available from the corresponding author on reasonable request.

⁵Department of Pathology, Tisch Cancer Institute, Icahn School of Medicine at Mount Sinai, New York, NY, USA.

⁶Cancer Biology Program, Beth Israel Deaconess Medical Center, Harvard Medical School, Boston, MA, USA.

⁷Department of Cancer Biology and Genetics, Memorial Sloan Kettering Cancer Center, New York, NY, USA.

⁸Department of Thoracic/Head & Neck Medical Oncology, The University of Texas MD Anderson Cancer Center, Houston, TX, USA.

⁹Department, Antitumor Assessment Core and Molecular Pharmacology Memorial Sloan Kettering Cancer Center, New York, NY 10065.

[†]Institute of Molecular and Cellular Biosciences, The University of Tokyo, Tokyo, Japan.

[‡]Albert Einstein College of Medicine, Bronx, NY, USA.

[§]Department of Oncology and Metabolism, The University of Sheffield, Sheffield, UK.

[¶]Hofstra-Northwell School of Medicine and Cold Spring Harbor Laboratory, Hempstead, NY, USA.

Abstract

Drug-based strategies to overcome tumour resistance to radiotherapy (R-RT) remain limited by the single-agent toxicity of traditional radiosensitizers (e.g., platinum) and a lack of targeted alternatives. In a screen for compounds that restore radiosensitivity in *p53* mutant zebrafish while tolerated in non-irradiated wild-type animals, we identified the benzimidazole anthelmintic, oxfendazole. Surprisingly, oxfendazole acts via inhibition of IRAK1, a kinase otherwise involved in Interleukin-1 and Toll-like receptor (IL-1R/TLR) immune responses. IRAK1 drives R-RT in a pathway involving IRAK4 and TRAF6 but not the IL-1R/TLR—IRAK adaptor MyD88. Rather than stimulating NF- κ B, radiation-activated IRAK1 acts to prevent apoptosis mediated by the PIDDosome complex (PIDD/RAIDD/caspase-2). Countering this pathway with IRAK1 inhibitors suppresses R-RT in tumour models derived from cancers in which *TP53* mutations predict R-RT. Lastly, IRAK1 inhibitors synergize with inhibitors of PIN1, a prolyl isomerase essential for IRAK1 activation in response to pathogens and, as shown here, ionizing radiation. These data identify an IRAK1 radiation-response pathway as a rational chemo-RT target.

Introduction

RT delivers cytotoxic DNA breaks to tumor cells while minimizing damage to healthy tissues, and is given to ~60% of cancer patients over the course of treatment^{1,2}. Current approaches to overcoming tumor R-RT consist of concurrent systemic chemotherapy with classical anticancer agents such as genotoxins (e.g., cisplatin, 5-FU) and microtubule inhibitors (e.g., taxanes). These traditional radiosensitizers primarily act by augmenting DNA damage levels, thus enhancing cell killing within the field of radiation¹⁻⁴.

Radiosensitizers can be effective: cisplatin-based chemoradiation therapy (CRT) improves survival by 10% compared to RT alone in patients with head and neck squamous cell carcinoma (HNSCC) and is the current standard of care in this cancer⁵. However, tumors

recur in a large majority of patients, leading to invariably fatal disease. Further improvements of CRT have remained limited by the toxicity of radiosensitizers as single-agents^{2,3}. Moreover, these genotoxic drugs were not designed against –and thus do not necessarily target– the genetic defects or signaling pathways that drive tumor R-RT. Devising targeted strategies to supplant these cytotoxic chemotherapies is a current central focus of NCI's Radiation Therapy Oncology Group (NCI-RTOG) and NCRI's Clinical and Translational Radiotherapy Research Working Group (CTRad, UK)².

A candidate, potentially pervasive mechanism of tumor R-RT is mutation of the p53 transcription factor, which occurs in ~50% of solid tumors⁶. Cells with mutant p53 fail to initiate apoptotic or senescence gene-expression programs in response to ionizing radiation (IR)-induced DNA breaks^{7–9}. In HNSCC^{10,11}, colorectal cancer (CRC)^{12,13}, breast cancer (BC)¹⁴, glioblastoma (GBM)¹⁵ and medulloblastoma (MB)¹⁶, patients with missense *TP53* mutations have markedly worse outcomes following RT or CRT compared to patients with WT *TP53*, with declines in recurrence-free or overall survival ranging from ~33% to 100%. Yet, patients are not stratified by *TP53* status and there are currently no drugs reported to improve RT outcomes in *TP53* mutant tumors^{1,2}.

Results

***In vivo* zebrafish radiosensitizer screen identifies oxfendazole.**

To identify such genotype-directed radiosensitizers while accounting for the problem of systemic toxicity, we developed a whole-animal model of mutant *TP53*-driven R-RT for use in unbiased genetic and chemical screens^{17,18}. In this model, zebrafish embryos homozygous for the M214K (MK) mutation in *tp53* display fully penetrant R-RT, as evidenced by (i) a complete lack of cell death induction in response to IR, a phenotype scored in 24–48 hours post fertilization (hpf) embryos (Supplementary Fig. 1a-b)^{17,18}; and, (ii) a complete lack of IR-induced dorsal tail curvatures (DTC), a morphological manifestation of zebrafish radiosensitivity¹⁹ assessable by eye in 96–120 hpf larvae (Fig. 1a). The mutated M214 residue corresponds to M246 in human p53, which maps to the mutational hot-spot region in the DNA-binding domain and is mutated in >150 human tumors sequenced thus far⁶. In a pilot, candidate gene-based screen, we found that inhibitors of checkpoint kinase 1 (Chk1) such as Gö6976 restore wild-type (WT) levels of IR-induced cell death in *p53^{MK/MK}* embryos, with minimal toxicity in the absence of IR (Supplementary Fig. 1a-b)¹⁸. Such potent radiosensitization by Chk1 inhibitor is also evident in the late DTC assay, whereby Gö6976 restores DTC formation in ~75% of the mutants with no effects in the absence of IR (Fig. 1a,b and Supplementary Fig. 1d). Gö6976 thus provided a positive control for large-scale radiosensitizer screens exploiting the morphological DTC phenotype as readout.

In a screen of 1,151 small molecules (including 640 FDA-approved drugs), we identified one compound, oxfendazole, which radiosensitized *p53^{MK/MK}* mutants with both greater potency and lesser toxicity than Gö6976 (Fig. 1b, Supplementary Fig. 1c-g, and Supplementary Tables 1 and 2). Importantly, these effects were observed at concentrations tolerated by non-irradiated WT embryos (Fig. 1c). Radiosensitization by oxfendazole was retained in mutant p53-depleted *p53^{MK/MK}* embryos (Supplementary Fig 2a-c); was

apoptotic in nature, as evidenced by acridine orange, TUNEL and active caspase-3 stains of 48 hpf embryos examined 30 hours post-IR (hpIR) (Fig. 1d); associated with an increase in DNA damage levels (Supplementary Fig. 2d-e); and was dose- and time-dependent, with maximal efficacy when administered 0–4 hpIR (Supplementary Fig. 2g-i).

Target discovery for oxfendazole identifies IRAK1.

Oxfendazole is a benzimidazole anthelmintic approved for the treatment of worm infections in livestock^{20,21}. Because other microtubule inhibitors such as taxanes are commonly used as radiosensitizers⁴, we initially considered tubulin inhibition as the mechanism for oxfendazole-mediated radiosensitization. Unexpectedly, none of seven tubulin-binding analogs of oxfendazole, including the classic antimetabolic nocodazole, could phenocopy the drug (*in vivo* SAR shown in Fig. 1e). Specifically, while the analogs could produce DTCs as efficiently as oxfendazole, none showed any selectivity for IR (with the possible exception of ricobendazole) and induced DTCs in the mutants regardless of radiation (Fig. 1e). Thus, tubulin inhibition is unlikely to fully account for, if even involved in, oxfendazole's radiosensitizing properties. It is notable in this regard that of all benzimidazoles tested, oxfendazole and ricobendazole have the lowest affinity for tubulin²⁰.

To identify novel target(s) of oxfendazole whose inhibition might drive radiosensitization, we used the Similarity Ensemble Approach (SEA) target-prediction algorithm (Fig. 2a)²². SEA yielded 12 candidate targets, which we then tested for their ability to phenocopy oxfendazole when inhibited by specific inhibitors *in vivo* (Figs. 2b and Supplementary Fig. 2j). This analysis identified Interleukin-1 Receptor-Associated Kinases IRAK1 and IRAK4^{23,24}, whose inhibition by IRAK1/4 kinase inhibitor (IRAK1/4i)²⁵ radiosensitized *p53^{MK/MK}* embryos with a potency nearing that of oxfendazole (Fig. 2b-d, 3a and Supplementary Fig. 2j). Kinase-binding and *in vitro* kinase assays demonstrated oxfendazole as a selective IRAK1 inhibitor (Fig. 2h and 2i, respectively). The observed K_d (5.8 μ M) and IC_{50} (38 μ M) were consistent with concentrations of oxfendazole that radiosensitize zebrafish *p53^{MK/MK}* mutants (Fig. 1e). Docking of oxfendazole onto IRAK4-derived zebrafish and human IRAK1 models²⁶ predicts drug binding to the ATP-binding site and an interaction with the hinge region via the benzimidazolyl carbamate moiety, while the phenylsulfoxide moiety resides in a pocket adjacent to the DFG-motif (Fig. 2e-g).

IRAK1 is known as an effector of IL-1R and TLRs in innate immune signaling²⁷. It acts through the TRAF6 E3 ubiquitin ligase to stimulate NF- κ B, p38/MAPK, JNK and ERK pro-survival and inflammatory responses to pathogens^{23,24}. IRAK1 had not been previously implicated in the DNA damage response or cellular response to RT. Yet inspection of The Cancer Genome Atlas (TCGA) cohort revealed significant overexpression of *IRAK1* in HNSCC and BC patient samples of *TP53* mutant genotype compared to WT, as well as tumors from those BC patients that ultimately received RT as part of their treatment (Supplementary Fig. 3a,i-j; $P < 0.0001$, $P < 0.0001$ and $P < 0.05$, respectively; Wilcoxon rank-sum test). We also found that IRAK1 is commonly activated in response to IR in *TP53* mutant HNSCC, BC and CRC –derived cell lines, correlating with pronounced R-RT phenotypes (Fig. 5d,g,h). We thus further investigated IRAK1 as a target for inhibition in tumor R-RT.

We first sought to confirm the oxfendazole and IRAK1/4i data with additional IRAK1 inhibitors and gene targeting in zebrafish *p53^{MK/MK}* embryos, as well as *TP53* mutant human cancer cells. For IRAK1 inhibition, we selected the tyrosine kinase inhibitor R406, which inhibits IRAK1 with an IC₅₀ of 9.7 nM vs. 150 nM for IRAK4²⁸; and Ginsenoside-Rb1 (Gin-Rb1), a ginseng extract that inhibits IRAK1 but not IRAK4 or IRAK2²⁹. Whether in zebrafish *p53^{MK/MK}* mutants, HeLa cells (devoid of p53 protein via HPV E6) or *TP53* mutant or null human cancer cell lines, genetic or pharmacologic inhibition of IRAK1 was consistently incompatible with cell survival in the presence of IR but tolerated in the absence of IR (Figs. 2j, 3a-f, 4a, 5e and Supplementary Fig. 4a-f). Both the zebrafish and human-cell *IRAK1* knockdown models were rescued by WT but not kinase dead³⁰ (KD) human IRAK1 (Figs. 3e-g and 4c). Importantly, overexpression of WT, but not KD, IRAK1 was sufficient to confer R-RT to otherwise radiosensitive Daoy MB cells (Fig. 4b). Finally, CRISPR/Cas9 gene-editing confirmed the kinase's essential requirement for cell survival specifically after IR (Fig. 4d).

IRAK1 drives R-RT independently of its IL-1R/TLR adaptor, MyD88, and canonical downstream pathways.

Both IRAK1's proximal activator and proximal effector in IL-1R/TLR signaling—IRAK4 and TRAF6, respectively^{23,24,27}—were also required for cell survival after IR (Fig. 4e). IRAK4 was necessary for IR-induced activation of IRAK1, as assessed by T209 phosphorylation^{31,32} (Fig. 4f), while an IRAK1 mutant deficient in TRAF6-binding, IRAK1^{E3A} (E544A/E587A/E706A)³³, afforded an only partial rescue of *irak1*-depleted *p53^{MK/MK}* embryos (Fig. 3e-g). By contrast, the adaptor protein MyD88—which bridges IRAK1/4 to IL-1R/TLRs and is essential for IRAK1/4 activation in innate immunity^{23,24,27,34}—was dispensable for both IR-induced IRAK1 T209 phosphorylation and overall R-RT in HeLa cells and *p53^{MK/MK}* zebrafish (Figs. 4e-i and Supplementary Fig. 4g,k,l). In further contrast with canonical IRAK1 immune signaling: (i) the kinase did not engage NF- κ B, p38/MAPK, JNK or ERK signaling in response to IR (Figure 4j and Supplementary Fig. 4h); and, (ii) an IRAK1 mutant deficient in NF- κ B essential modulator (NEMO) binding, IRAK1^{K2R} (K134R/K180R)³⁵, restored R-RT in *Irak1*-depleted *p53^{MK/MK}* zebrafish as efficiently as WT IRAK1 (Fig. 3e-g).

IR-activated IRAK1 acts to suppress PIDDosome-mediated apoptosis.

Instead of acting through its aforementioned canonical signaling pathways, we found that IRAK1 drives survival after IR by preventing PIDDosome (PIDD-RAIDD-caspase-2) signaling, a DNA damage-inducible apoptotic axis that does not require p53 for activation or function after IR³⁶⁻³⁸. Indeed, depletion or deletion of IRAK1 triggered caspase-2 (C2) maturation in irradiated cells in a *PIDD*- and *RAIDD*-dependent manner (Fig. 4k-l and Supplementary Fig. 4i-j), and IRAK1 inhibitor-mediated radiosensitization was abolished in *PIDD*-, *RAIDD*- and C2-depleted cells³⁶ (Fig. 4m-n). As expected from previous studies^{36,39}, PIDDosome-mediated radiosensitization associated with increased levels of DNA damage (Supplementary Fig. 2f). Lastly, IRAK1 inhibition after IR was sufficient to enable ATM-mediated phosphorylation of the PIDD death domain (PIDDpT788, Figure 4k and Supplementary Fig. 4i), an event necessary and sufficient for RAIDD recruitment and PIDDosome formation³⁶. Altogether, the data pointed to an evolutionarily conserved role for

IRAK1 in protecting cells from IR-induced cell death, acting in a pathway related to, but genetically distinct from, IL-1R/TLR signaling.

IRAK1 inhibitors restore radiosensitivity in multiple cell models of tumour R-RT.

To evaluate the robustness of the IRAK1-targeting strategy, we analyzed the radiosensitizing properties of IRAK1 inhibitors across both tumor- and *TP53*-mutation spectrums. We assembled a panel of relevant cancer cell lines based on three criteria: cell lines must (i) originate from a tumor type in which *TP53* mutations adversely affect patient survival after RT or CRT; (ii) contain a non-synonymous mutation in *TP53*; and (iii) have been previously demonstrated as radioresistant in clonogenic assays. A search of the Cancer Cell Line Encyclopedia⁴⁰ combined with a literature search identified 12 such lines derived from HNSCC, MB, GBM, CRC and BC (Fig. 5d). We also included MCF7 cells, which while WT for *TP53* display profound resistance to IR due to deletion of *CASP3*⁴¹. With the exception of the MB Daoy line, all selected cell lines confirmed as radioresistant in response to 2.5, 5 and up to 7.5 Gy IR (Fig. 5b-d and Supplementary Fig. 5, DMSO columns and corresponding cell viability curves, respectively). We thus screened the panel with the IRAK1 inhibitors R406 and Gin-Rb1 applied at their respective MTDs, as determined in HeLa cells (Fig. 5a), as well as a two-fold higher dose. For comparison, we tested cisplatin (MTD and 2xMTD, as above), whose combination with RT is a standard of care in HNSCC and is commonly used in CRT of many other cancers². Cisplatin failed to sensitize any of the *TP53* mutant lines to IR, with only marginal additive effects observed in YD38 and T98G cells (Fig. 5d and Supplementary Fig. 5). In stark contrast, Gin-Rb1 and R406 radiosensitized up to 10 and 7 of 11 *TP53* mutant lines, respectively (Daoy excluded) (Fig. 5d and Supplementary Fig. 5 for corresponding cell viability curves; Supplementary Fig. 4d-f for select colony assays). MCF7 radioresistance could not be overcome throughout the screen regardless of drug, drug dose or IR dose. In the great majority of cases, radiosensitization by the IRAK1 inhibitors occurred in those lines that engaged IRAK1 T209 phosphorylation in response to IR (Fig. 5g-h), and was obtained at drug doses that were tolerated: (i) in the absence of IR (see 0 Gy data points in Fig. 5d and Supplementary Fig. 5); and (ii) in irradiated non-tumorigenic fibroblasts (IMR-90) and mammary epithelial cells (MCF10A) (Fig. 5f and Supplementary Fig. 5). Taken together with the zebrafish and HeLa data, these results identified IRAK1 as a target for inhibition in cancers with mutant *TP53*-driven R-RT.

An additional predicted oxfendazole target, PIN1 isomerase, drives R-RT in zebrafish and tumour-cell models and associates with R-RT in HNSCC.

Upon our analysis of SEA-predicted oxfendazole targets, we noticed that inhibition of one additional candidate target, the peptidyl-prolyl *cis/trans* isomerase PIN1⁴², radiosensitized zebrafish *p53*^{MK/MK} mutants with similar potency to that of IRAK1/4i (Fig. 2a-b). While *in vitro* isomerase and thermal shift assays could not immediately confirm PIN1 as an oxfendazole target (Supplementary Fig. 6a-b), genetic or pharmacologic inhibition of PIN1 did consistently suppress R-RT in zebrafish (Fig. 6a-b and Supplementary Fig. 6c-g), HeLa cells (Fig. 6c and Supplementary Fig. 6i-j), and HNSCC lines (Fig. 6e-f, Supplementary Fig. 6n for corresponding cell viability curves, and Supplementary Fig. 6j-m for select colony assays). Like IRAK1, PIN1 was sufficient to force R-RT when overexpressed in

radiosensitive Daoy cells whereas a catalytically inactive (W34A/K63A) variant⁴³ was less potent (Fig. 6d). In further support of PIN1 as a driver of tumor R-RT, overexpression of *PIN1* significantly associated with locoregional recurrence (LRR; $P=0.006$) and reduced overall survival (OS; $P=0.007$), but not distant metastases (DM), in HNSCC patients of *TP53* mutant genotype that were treated with post-operative RT at the MD Anderson Cancer Center^{11,44} (Fig. 6g-j and Supplemental Table 3). Inspection of the TCGA HNSCC cohort – whose analysis is however limited by a lack of LRR data⁴⁵ – revealed significant upregulation of *PIN1* in *TP53* mutant tumors that were ultimately treated with RT (Supplementary Fig. 3f-h).

PIN1 inhibition prevents IR-induced IRAK1 activation and synergizes with IRAK1 inhibitors *in vitro* and *in vivo*.

Interestingly, PIN1 plays an essential and direct role in TLR-induced IRAK1 activation⁴⁶. Likewise, we found that genetic or pharmacologic inhibition of PIN1 blocked IR-induced IRAK1 phosphorylation on T209 (Fig 6k-l). We thus tested whether IRAK1 and PIN1 inhibitors synergistically suppress R-RT in our various models. We trialed four combinations of IRAK1+PIN1 inhibitors, involving the IRAK1 inhibitors Gin-Rb1 and R406 (see above), and the PIN1 inhibitors epigallocatechin gallate (EGCG), a competitive inhibitor with μM efficacy shown to bind the PIN1 catalytic site^{47,48}; and buparvaquone, a repurposed antiparasitic which binds and inhibits PIN1 with nM efficacy⁴⁹. Each inhibitor was titrated to a dose that did not decrease HeLa survival as single agent, even after 2.5 or 5 Gy IR. Under these subtherapeutic conditions, all four combination treatments produced marked synergistic declines in survival specifically after IR (Fig. 7a; Supplementary Figs. 7a and 7e for combination indexes). These findings were recapitulated in: *p53^{MK/MK}* fish (Fig. 7c and Supplementary Figs. 6h and 7f); *TP53* mutant HNSCC cell lines grown *in vitro* (Fig. 7d and Supplementary Figs. 7b-d,g) or as tumor xenografts *in vivo* (Fig. 7e-g and Supplemental Fig. 7h); *TP53^{-/-}* as well as WT HCT116 cells (Supplementary Fig. 7i); and one of the cell lines from our radioresistant panel that best resisted IRAK1 inhibitors as single agents (SW480 cells, Supplemental Fig. 7b,g). All four IRAK1i+PIN1i combinations were otherwise tolerated in IMR90 human fibroblasts, including after up to 7.5 Gy IR (Fig. 7b, left). While MCF10A mammary epithelial cells showed some sensitivity (Fig. 7b, right), such toxicity was not further exacerbated by IR and was marginal compared to the levels of tumor-cell lethality induced by the various drug combinations in the tumorigenic cell lines (e.g., compare 5 Gy data points in panel 7b vs. that in Supplemental Fig. 7a-b). Clinical translation will require extending these studies to additional *in vivo* tumor models/*TP53* alleles, including in immunocompetent mice. Altogether, our data collectively identify IRAK1 and PIN1 as rational targets in radioresistant cancers with efficacy stemming from single or low-dose combination treatments.

Discussion

The data presented here show that IRAK1 kinase, a core transducer in innate immune signaling conserved from flies to man^{23,24,27}, plays an additional conserved role in the cell survival response to IR. While this pathway involves the IL-1R/TLR pathway members PIN1, IRAK4 and TRAF6, its MyD88-independence, full reliance on IRAK1 kinase activity,

partial reliance on TRAF6, and divergent downstream target (the PIDDosome) are supportive of a distinct stress-response pathway that diverged from, or possibly preceded, the pathogen response. The pathway may respond to one or more IR-induced primary or secondary ionization events, including DNA breakage, micronucleation or other occurrences of cytosolic DNA, hydroxyl radicals or other reactive oxygen species, ruptured lipid bilayers, and/or so-called Danger Associated Molecular Patterns (DAMPs), i.e., DNA or nuclear proteins released into extracellular space^{50,51}. A key feature of this pathway from a therapeutic viewpoint is its IR-induced essentiality, whereby pathway inhibition is lethal to zebrafish or cancer cells exposed to IR but is otherwise tolerated in the absence of IR. Even germline losses of *Irak1* or *Pin1* are viable in mice^{52,53}. Thus, IRAK1±PIN1 inhibitor treatment could lead to improved tumor radiosensitization strategies whereby drug-induced cytotoxicity is restricted to the field of RT with minimal effects in unexposed tissues. Additionally, the radiosensitizing properties of IRAK1 and PIN1 inhibitors in *TP53* mutant tumor cells are not allele-specific and are largely retained in *TP53*^{-/-} and WT backgrounds. This potentially expands the patient population that might benefit from IRAK1±PIN1 inhibitor-based CRT. Lastly, recent reports implicate deregulated *IRAK1* and *PIN1* in tumor progression, maintenance and metastasis, via stabilization of mutant p53 itself⁵⁴ and other pathways^{23,32,34,42}. Our discovery of these enzymes as drivers of cellular R-RT calls for further development of IRAK1 and PIN1 inhibitors for therapeutic use.

Methods

Zebrafish Lines and Maintenance

Adult zebrafish were maintained on a 14:10 hour light:dark cycle at 28°C in accordance with the regulations and policies of the Mount Sinai Institutional Animal Care and Use Committee. The study is compliant with all relevant ethical regulations regarding zebrafish research. The progeny of *p53*^{M214K/M214K} fish were used in most experiments. Wild-type zebrafish were from the AB line. The TILLING-mediated generation of the *p53*^{M214K/M214K} line, including allele designation, has been described^{17,18}.

Zebrafish Drug Screen

Live embryos were dechorionated in pronase (2.0 mg/mL in egg water) for 7 minutes and rinsed three times in egg water at 17 hpf. At least 15 *p53*^{M214K/M214K} embryos were then arrayed into each well of a 24-well plate and treated with drugs from FDA-approved drug library V1 (Enzo Life Sciences) or proprietary kinase inhibitors (Reddy Lab) at a final concentration of 20 µg/mL in egg water. In the primary screen, three wells were set aside for controls: one negative control: *p53*^{M214K/M214K} + DMSO; two positive controls: *p53*^{M214K/M214K} + Gö6956 (1 µM), *p53*^{+/+} + DMSO. Plates containing drug-treated embryos were γ-irradiated at 18 hpf using a ¹³⁷Cs-irradiator (X-ray IR can also be used but developmental stage and dose differ, presumably due to low-energy electrons). 6 hours post IR (hpIR), embryos were washed three times and scored at 72 hpf and 120 hpf for curved tails and gross morphological changes. If any well lost embryos to necrosis or manipulation such that less than 12 embryos were left before 120 hpf, that data point was not included in analysis and the entire condition was repeated. In the secondary screen, set-up was similar except two 24-well plates were set-up with identical drug treatments identified in the

primary screen, with embryos randomly assigned to each plate. Phenotyping was identical to the primary screen. Again, at least 12 embryos were required to survive until 120 hpf for the data point to be counted and the secondary screen was performed in three independent experiments. Pictures were obtained of tricaine-anesthetized embryos mounted on 2–3% methylcellulose and imaged with a Nikon SMZ 1500 fluorescence microscope.

Acridine Orange (AO) Labeling.

Live embryos were dechorionated in pronase (2.0 mg/mL in egg water) for 7 minutes and rinsed three times in egg water at 17 hpf. After being arrayed and incubated with drugs, depending on the experiment, embryos were then γ -irradiated at 18hpf using a ^{137}Cs -irradiator. 6 hours post IR (hpIR), embryos were labeled live with AO at 10mg/mL in egg water for 20 min, washed three times, and analyzed with ImageJ as previously described¹⁸.

Whole-mount TUNEL Staining and Caspase-3 Immunohistochemistry

The TUNEL cell death assay was performed according to manufacturer's instructions (ApoTag Fluorescein In Situ Apoptosis Detection Kit) with zebrafish manipulations as previously described¹⁸. Embryos stained for caspase-3 or γH2AX were fixed in 4% PFA overnight at 4°C and subsequently dehydrated in methanol at -20°C for at least 2 hours. Embryos were then rehydrated three times 5 min in PBST (1x PBS, 0.1% Tween-20), and permeabilized by treatment with PDT (PBST + 1% DMSO) supplemented with 0.3% Triton-X for 20 min. Embryos were treated with blocking solution (PDT supplemented with 10% heat inactivated FBS) for 30 min before the addition of primary antibody (anti-activated-Casp-3 1:500, StressGen AAs-103; anti- γH2AX 1:200, Millipore 05-636). Embryos were incubated in primary antibody overnight at 4°C, rinsed three times 20 min in PDT and then re-blocked for 30 min in blocking solution before the addition of AlexaFluor-conjugated secondary antibody (1:250). Immunohistochemistry for TUNEL and caspase-3 labeled embryos were imaged with a Nikon SMZ 1500 fluorescence microscope. Immunohistochemistry for γH2AX was imaged with a Leica SP5 DM confocal microscope.

Similarity Ensemble Approach (SEA) Analysis

Chemical compound SMILES formulas were queried with the online SEA search tool (<http://sea.bkslab.org/search/>) searching against ChEMBL version 16 Binding 10 μM . Results found benzimidazoles were copied into Microsoft Excel, sorted for duplicates, and color graded according to E-values.

TCGA Analysis

TCGA datasets for two cancer types (HNSCC, BRCA) were obtained from the Broad Institute's Firehose pipeline. Gene expression data was quantile normalized via RSEM and \log_2 transformed prior to analyses for IRAK1 and PIN1. *TP53* mutation status and radiation therapy treatment are summarized for each cancer type. Wilcoxon rank-sum test was performed to test the association between gene (IRAK1, PIN1) expression and *TP53* mutation status and receipt of radiation therapy. We further analyzed IRAK1/PIN1 expression in *TP53* mutant and WT groups, across patients that received radiotherapy versus those that did not. Survival comparisons were made via log rank test. Each gene was

stratified with respect to its median expression across *TP53* status to determine any prognostic association. All analysis was done in R software version 3.4.2 including the ‘survival’ package. Receipt of radiation is a time varying covariate which can confound survival association through the time it was administered. Date of receipt of radiation is needed to perform this analysis, which is not included in the TCGA data set⁵⁵.

Chemicals and Inhibitors

Oxfendazole, fluocinolone, exemestane, cefepime, pranlukast, amiloride, alfacalcidol, and albendazole were obtained from VWR; amoxapine, ricobendazole, mercazole were obtained from Sigma-Aldrich; Salmeterol, indomethacin, canthaxanthin, bifonazole, rapamycin, mebendazole, fenbendazole, and flubendazole were obtained from Santa Cruz Biotechnologies; misoprostol was obtained from Thermo Fisher; rebastinib and regorafenib were obtained from Selleck Chem; Gö6976 was obtained from Calbiochem. Lapatinib, SB203580, and SB202190 were gifted from Julio Aguirre-Ghiso. Debrafinib, sorafenib, and vemurafenib were gifted from Arvin Dar. Recombinant Human IL-1 β was from Peprotech (#200–01B) Doxycycline hyclate/doxycycline hyclate was purchased from SIGMA (#D9891–1G). Inhibitors used were IRAK1/4 Inhibitor (SIGMA #I5409), R406 (Selleck Chemicals #S2194), Ginsenoside-Rb1 (Abcam ab142646 and J&K Scientific #112127), Buparvaquone (Santa Cruz Biotechnology sc-210970) and EGCG (SIGMA #E4268 and #E4143). IRAK1/4 inhibitor was originally discovered in a high-throughput small-molecule screen for IRAK inhibitors, with IC₅₀ values 300 nM and 200 nM for IRAK1 and IRAK4 respectively. For 27 other kinases tested during discovery, IC₅₀ values were >10,000 nM²⁵. Ginsenoside Rb1 was originally isolated from ginseng extract and identified as a saponin among other components extracted from ginseng. It inhibits IRAK1 in an in vitro kinase assay with an IC₅₀ ~10 μ M²⁹, with other reported activities against PI3K/Akt, ER- β and enhancing the Nrf2/Ho-1 pathway among others. R406 was originally found to be a SYK inhibitor with a K_i of 30 nM⁵⁶, though DiscoverX assays (described above) showed it to also inhibit FLT3, as well as IRAK1 and IRAK4. EGCG was identified as a polyphenolic compound found in green tea with its earliest effects proposed to be a protectant against the carcinogenic effects of teleocidin and okadaic acid⁵⁷. It was later found to directly bind and inhibit PIN1 with a K_i of 20 μ mol/L⁴⁸. Buparvaquone was derived from a series of anti-*Theileria parva* (a cattle parasite) compounds, with its primary proposed mechanism as inhibiting the parasite cytochrome b. It was recently found to also inhibit *Theileria annulata* PIN1 in vitro (no reported IC₅₀ or K_d)⁴⁹.

In Vitro Kinase-Binding Assays (KINOMEScan)

KINOMEScan assays (DiscoverX) were performed as follows: Kinase-tagged T7 phage strains were prepared in an E. coli host derived from the BL21 strain. E. coli were grown to log-phase and infected with T7 phage and incubated with shaking at 32°C until lysis. The lysates were centrifuged and filtered to remove cell debris. The remaining kinases were produced in HEK-293 cells and subsequently tagged with DNA for qPCR detection. Streptavidin-coated magnetic beads were treated with biotinylated small molecule ligands for 30 minutes at room temperature to generate affinity resins for kinase assays. The liganded beads were blocked with excess biotin and washed with blocking buffer (SeaBlock (Pierce), 1% BSA, 0.05% Tween 20, 1 mM DTT) to remove unbound ligand and to reduce

nonspecific binding. Binding reactions were assembled by combining kinases, liganded affinity beads, and test compounds in 1x binding buffer (20% SeaBlock, 0.17x PBS, 0.05% Tween 20, 6 mM DTT). Test compounds were prepared as 111X stocks in 100% DMSO. K_d s were determined using an 11-point 3-fold compound dilution series with three DMSO control points. All compounds for K_d measurements are distributed by acoustic transfer (non-contact dispensing) in 100% DMSO. The compounds were then diluted directly into the assays such that the final concentration of DMSO was 0.9%. All reactions performed in polypropylene 384-well plates. Each was a final volume of 0.02 ml. The assay plates were incubated at room temperature with shaking for 1 hour and the affinity beads were washed with wash buffer (1x PBS, 0.05% Tween 20). The beads were then re-suspended in elution buffer (1x PBS, 0.05% Tween 20, 2 μ M non-biotinylated affinity ligand) and incubated at room temperature with shaking for 30 minutes. The kinase concentration in the eluates was measured by qPCR.

In vitro Kinase Assays

In vitro kinase assays were performed by Reaction Biology Corporation (Malvern, PA). Briefly, substrate (MBP, 20 μ M final) was freshly prepared in reaction buffer (20 mM Hepes pH 7.5, 10 mM MgCl₂, 1 mM EGTA, 0.02% Brij35, 0.02 mg/ml BSA, 0.1 mM Na₃VO₄, 2 mM DTT, 1% DMSO). 4 nM human IRAK1 kinase was added to the substrate solution, followed by oxfendazole by Acoustic technology (Echo550; nanoliter range). Samples were incubated for 20 min at room temperature before addition of ³³P-ATP (10 μ M final, specific activity of 10 μ Ci/ μ L), the incubated for 2 hr at room temperature. Radioactivity was detected by filter-binding method. Kinase activity data were expressed as the percent remaining kinase activity in test samples compared to vehicle (DMSO) reactions. Oxfendazole was tested in 10-dose IC₅₀ mode in triplicate with 3-fold serial dilution starting at 200 μ M, Control compound staurosporine was tested in 10-dose IC₅₀ mode with 4-fold serial dilution starting at 20 μ M. IC₅₀ values and curve fits were obtained using Prism (GraphPad Software).

Molecular Docking.

Protein sequences of IRAK1 and IRAK4 catalytic domain were aligned with T-Coffee's structure-based alignment mode, Expresso⁵⁸. IRAK4 x-ray structure (2nru)²⁶ was used as template for homology modeling of IRAK1. The homology modeling program MODELLER v9.15⁵⁹ was used to generate 10 IRAK1 models with an average ZDOPE⁶⁰ score of -0.64 ± 0.06 , suggesting that at least 70% of the atoms are within 3.5 Å of the native IRAK1 structure. Molecular docking to the IRAK1 models was performed with Glide, using the Standard Precision mode and a hydrogen-bond constraint at the hinge region. The docking results from the models were combined to generate the consensus docking result⁶¹. Oxfendazole and analogs are predicted to dock to the ATP-binding site and interact with the hinge region with the benzimidazolyl carbamate moiety, while the benzylsulfoxyl moiety in a pocket adjacent to the DFG-motif. Method for zebrafish IRAK1 homology modeling was the same as for human IRAK1. Default settings were used for Induced-fit Docking of Oxfendazole. Specifically, the scaling of van der Waals radii for receptor atom was changed to 0.75 for atoms with charge larger than $\pm 0.15 e$ ⁶².

Microinjections into Zebrafish Embryos

Human IRAK1 WT, KD and K134R/K180R were subcloned into the pCS2+ plasmid using restriction enzymes EcoRI and XhoI. The IRAK1 E3A-pCS2+ construct was generated using the Q5 site-directed mutagenesis Kit (NEB, #E0552S) to produce the E544A/E587A/E706A variant⁶³. All plasmids were linearized by Sac2 single enzyme treatment at 37°C for 4 hrs. Digests were stopped by adding 1/20 volume 0.5 M EDTA, 1/10 volume of 3 M Na acetate and 2 volumes EtOH. Samples were mixed and chilled at -20°C for 15 min, washed and resuspended in TE buffer. Sense-capped mRNAs were synthesized for injection using the mMESSAGE mMACHINE SP6 kit (Ambion, #AM1340) followed the manufacturer's instructions. mRNA concentrations were determined by Nanodrop and RNA gel. The following mRNAs were co-injected with *irak1* MO during the 1–2 cell stage: 20 pg WT IRAK1 mRNA, 25–30 pg IRAK1 KD, 25–30 pg K134R/180R or 25–30 pg E3A mutant mRNAs. *zp53*-ATG MO⁶⁴ and *zp53*⁶⁴ antibody (Genetex, GTX128135) were kindly provided by the Jaime Chu. Protein extractions from embryos was performed as previously described³ and analyzed by western blot as described later below. Morpholino (MOs) antisense oligonucleotides were obtained from Gene Tools, LLC. Sequences were as follows:

Standard control (“std”) 5' -CCTCTTACCTCAGTTACAATTTATA-3'

pin1-e1i1 5' -ACTCTCTCTGCTCACTCTGGATGAG-3'

irak1-i5e6 5' -AATCCTGCAACACAACAGCCACATT-3'

irak4-e4i4 5' -GTGAACAGGTAAAGCCTCACAGGAT-3'

zp53-ATG 5' -GCGCCATTGCTTTGCAAGAATTG-3'

myd88 5' -TCTTGACGGACTGGGAAACTC G-3'

MOs were resuspended in sterile water to a stock concentration of 2 mM and delivered into one-cell stage zebrafish embryos by microinjection at various final concentrations with 0.1% Phenolred (Sigma).

Sequencing primers for confirming knockdown:

rpp0-F: TAGCCGATCCGCAGACACAC

rpp0-R: CTGAACATCTCGCCCTTCTC

pin1-e1-F: AGAACATCACACGCAGCAAAG

pin1-e3-R: GTGCAAATGAGGCGTCTTCAA

irak1-e1-F: GGGTTATGGACTCGCTTTCA

irak1-e11-R: CATGCGAGGTCTCTTCTTC

Myd88F: TCTTGACGGACTGGGAAACTCG

Myd88R: GATTTGTAGACGACAGGGATTAGCC

RT-PCR and Protein Extraction from Zebrafish Embryos

Embryonic RNA was isolated from 24–48 hpf embryos (>15 embryos/sample) using a standard Trizol method (250 μ L Trizol (Invitrogen), 50 μ L CHCl_3 , 175 μ L isopropanol). One microgram of purified RNA was used to generate cDNA using the Invitrogen SuperScript First Strand III RT-PCR kit, with oligo-dT primers. Two micrograms of the cDNA product is loaded on a 1% agarose gel. Pooled embryo protein lysates were harvested as previously described¹⁸.

Cell Culture and Cell Lines

HeLa, HCT116, CAL27, SAS, BHY, HN, and Detroit562 cell lines were cultured in DMEM medium (GIBCO) supplemented with 10% fetal bovine serum (FBS) and 1% penicillin/streptomycin. YD38 cells were cultured in RPMI medium, also supplemented with 10% FBS and 1% penicillin/streptomycin. Experiments requiring combined drug-treatment and irradiation were performed as follows: cells were seeded in 10cm plates and grown to 30–50% confluence. 1 hour before IR, cells were treated with drugs accordingly. Harvesting lysates for western blotting after IR typically occurred at 24 hpIR, while harvesting cells for fixation and TUNEL staining occurred after 48 hpIR. CAL27, Detroit562, Daoy, and T98G cells were obtained from ATCC. SAS cells were purchased from HSRRB, BHY from DSMZ, and YD38 from KCLB. MDA-MB-231, T47D, and MCF7 cells were kindly provided by Doris Germain. HeLa stable shPIDD, shRAIDD and shCASP2 cells have been described³⁶. IMR90 and MCF10A cells were kindly provided by Julio Aguirre-Ghiso. See Supplementary Table 3 for more details on cell line-specific culture media and protocols.

siRNA transfection, shRNA transduction, DNA transfection and constructs

siRNA transfections were performed using X-tremeGENE siRNA transfection reagent (Roche) and unless otherwise stated 20nM siRNA according to the manufacturer's instructions. Cells were exposed to IR +/- Gö6976 or oxfendazole at 48 hours post-transfection. Lentiviral shRNA transduction was performed in HeLa cells as previously described³⁶ with shTRIPZ, shPIN1, and shIRAK1. shPIDD, shRAIDD and shCASP2 HeLa cells and hairpin sequences have been described³⁶. DNA transfections were performed as previously described⁶⁵. Human IRAK1 WT and KD³⁰ were kind gifts from Dr Xiaoxia Li. IRAK1 Human IRAK1 K134R/K180R in pDEST-515 vector³⁵ was from Jonathan Ashwell. IRAK1 E3A, derived from WT IRAK1 template, was generated using the Q5 site-directed mutagenesis Kit (NEB, #E0552S) to produce the E544A/E587A/E706A mutations⁶³. pBybe-PIN1-WT and pBybe-PIN1-W34K63A have been described⁶⁶. siRNAs were also provided by Qiagen and target sequences were:

siIRAK1#5: CCGGGCAATTCAGTTTCTACA

siIRAK1#6: TCCCATCGCCATGCAGATCTA

siIRAK4#6: ATCCTATTAGTCATATATTTA

siMYD88#5: AACTGGAACAGACAAACTATC

siTRAF6#7: AGGGTACAATACGCCTTACAA

siPIN1#5: GACCGCCAGATTCTCCCTTAA

siPIN1#6: CAGTATTTATTGTTCCCACAA

shRNA clones were purchased from Quiagen and mature antisense sequences were:

shIRAK1: ATTACTCAAGGACAACCTG (V3THS_305359)

shPIN1.1: TGAAGTAGTACTACTCGGCC

shPIN1.2: TGGCTGAGCTGCAGTCGCT

CRISPR/Cas9 gene editing

Plasmid lentiCRISPR v2 was digested with BbsI (New England Biolabs Cat. No R0580) according to manufacturer' s recommendations, briefly: 1µg of plasmid was digested for 1h at 55°C, then digested plasmid was gel purified using QIAquick Gel Extraction Kit and eluted in water. sgRNA oligos for cloning were annealed by mixing them in equal 10 µM concentrations with addition of 1xT4 DNA Ligase Buffer, then mixture was incubated 37°C 30 min, then 95°C 5 min and then ramped down to 25°C at 5°C/min, hybridized oligos diluted 1:200 with H₂O. BbsI digested lentiCRISPR v2 plasmid (50ng) was ligated with 1 µM final concentration oligo duplex using T4 Ligase (NEB Cat. No. M0202) according to manufacturer' s recommendations and incubated overnight at 4°C. XL-1 blue competent *E. coli* were transformed with 1 µl of ligation reaction according to manufacturer' s protocol (Cat. No. 200249). Single clones were sequence verified using Sanger sequencing. Lentivirus particles containing sgRNA constructs of IRAK1 were generated by transfecting Phoenix packaging cells with lentiCRISPR v2 containing IRAK1 sgRNAs and combination of lentiviral helper plasmids pCMV-dR8.91 and pMD.G at a ratio of 2:1:1, respectively, jetPEI (101–10N; Polyplus) was used as transfecting agent. 24 hours later media containing viral particles was collected and concentrated using Lenti-X concentrator according to manufacturer' s protocol (Clontech Cat. No. 631231). Briefly, 1 volume of Lenti-X Concentrator mixed with 3 volumes of 0.45µm filtered viral particles containing media. Solution incubated overnight at 4°C. Then samples centrifuged at 1,500 x g for 45 minutes at 4°C, supernatant aspirated and pellet resuspended in HeLa and Cal27 cells growth media. For infection, 2×10⁵ HeLa and Cal27 cells plated into 6-well plates, next day 5µM polybrene (Millipore Cat. No. tr-1003-g) and 200µl of concentrated viral particles added per well. Next day media replaced with media containing 1µg/ml puromycin for selection.

IRAK1 sgRNA oligos (5' ->3') were:

sgRNA1:

- a. CACCGACACGGTGTATGCTGTGAAG
- b. AAACCTTCACAGCATAACACCGTGTC

sgRNA2:

a. CACCGAGGAGTACATCAAGACGGGA

b. AAACCTCCCGTCTTGATGTACTCCTC

sgRNA3:

a. CACCGATTTATCCCACAGAAAGACC

b. AAACGGTCTTTCTGTGGGATAAATC

sgRNA4:

a. CACCGGATCAACCGCAACGCCCGTG

b. AAACCACGGGCGTTGCGGTTGATCC

AlamarBlue Cell Survival Assay

Cells were seeded to 96-well plates at densities ranging from 400–1500 cells/well (see Supplementary Table 3 for seeding densities). 8 hours after seeding, if experiments were performed on cells without shRNA previously transfected, drugs were added to the medium, incubated 1 hour, then irradiated. If shRNA lines were used, cells were treated with 1 µg/ml doxycycline for 24 hours before irradiation. 3–4 days post IR, cells were incubated with AlamarBlue (ThermoFisher) at a final concentration of 10%. Absorbance was measured at a wavelength of 570 nm with a 600 nm reference wavelength. Relative fluorescence (RFU) was calculated using cell free wells as a control reference and percent survival was calculated compared to DMSO-treated, non-irradiated controls.

Clonogenic Assay

Single-cell suspensions were seeded into 6-well plates (50–200 cells/well). Drugs were added to the medium after 8 hours and irradiated in a ¹³⁷Cs-irradiator. After being cultured for 14 days, plates were rinsed with PBS, incubated with fixing solution (75% methanol, 25% acetic acid) and stained by 0.5% crystal violet (Sigma-Aldrich, St Louis, MO, USA) in methanol for 30 min at room temperature. Colonies consisting of at least 50 cells were scored. Clonogenic assays performed on shRNA transfected lines required refreshing media with 1 µg/ml doxycycline every 48 hours.

TUNEL Assay (cell lines)

TUNEL assays in HeLa cells were performed using the APO-BRDU kit (BD Biosciences) as described previously¹⁸.

Western Blotting and Antibodies

Whole-cell lysates were prepared in RIPA buffer or 1% NP-40 Buffer (Boston BioProducts). Lysate (25–200 µg) was added to NuPAGE LDS Sample Buffer (4X) (Invitrogen) and 5% 2-Mercaptoethanol (Sigma), and samples were incubated at 70°C for 10 min. Samples were run on a Tris-Acetate gel in MES Running buffer (Invitrogen). After electrophoresis, samples were transferred for 2 hr (90V, 150–200 mA) to a Nitrocellulose membrane (Thermo Scientific) using a submerged transfer apparatus (Bio-Rad). Membranes were then blocked with 5% bovine serum albumin (BSA) in Tris-buffered saline with 0.1% tween

(TBST) and probed overnight at 4°C with primary antibodies. Membranes were then washed in TBST and probed with anti-rabbit, -rat, or -mouse (Cell Signaling Technology) HRP-linked antibodies at a 1:2000–4000 dilution for 1 hr, washed, and placed in SuperSignal West Pico Chemiluminescent Substrate or SuperSignal West Dura Extended Duration Substrate (Pierce Biotechnology). The band of interest was then identified with photographic film. Antibodies were: α - γ H2AX (Ser139) (Cell Signaling Technology #9718), α -Chk1 (clone G-4, sc-8408), α -Chk1pSer345 (clone 13303, Cell Signaling Technology #2348), α -PIDD (anti-LRDD, clone Anto1, Novus Biologicals NBP1–97595), α -RAIDD (clone 4B12, MBL), α -PIDDpT788 (custom-generated, ref.31), α -caspase-2 (clone 11B4, EMD Millipore MAB3507), α -IRAK1 (Cell Signaling Technology #4504), α -IRAK1pT209 (Assay Biotech, #A1074), α -IRAK1pS376 (Genetex, #55332), α -IRAK4 (Cell Signaling Technology #4363), α -ERKpT202/Y204 (Cell Signaling Technology #4370), α -ERK1/2 (Cell Signaling Technology #4696), α -p38pT180/Y182 (Cell Signaling Technology #4511), α -p38 (BD Biosciences #610168), α -JNKpT183/Y185 (Santa Cruz sc-6254), α -I κ B α (Cell Signaling Technology #4814), α -TRAF6 (Santa Cruz sc-8409), α -MyD88 (Cell Signaling #4283), α -PIN1 (Abcam ab53350), α -actin (Abcam ab8227), α -Chk2 (clone 7, Millipore), α -p-Chk2 (T68) (#2661, Cell Signaling), α -GAPDH (Cell Signaling #2118), α -FLAG (DYKDDDDK Tag antibody, Cell Signaling Technology #2368),

Immunofluorescence and Confocal Microscopy (Cell Culture)

Hela cells (1×10^5) were seeded on coverslips in 6-well plates, fixed in 1% PFA, permeabilized in 0.2% Triton X-100, blocked in 1% BSA-PBS, stained with IRAK1 antibody 1:100 and secondary antibody 1:200 (anti-rabbit, Alexa Fluor 488, Invitrogen), mounted in vectashield with DAPI and sealed with nail polish, as described previously⁶⁵. Images were obtained under a 63X NA 1.40 oil objective with an invert confocal microscope (405 nm, 488 nm; SP5, Leica) and acquired using LAS software.

PPIase assay

The PPIase activity on GST-Pin1, GST-FKBP12, or GST-cyclophilin in response to compounds were determined using the chymotrypsin coupled PPIase activity assay with the substrate Suc-Ala-pSer-Pro-Phe-pNA, Suc-Ala-Glu-Pro-Phe-pNA or Suc-Ala-Ala-Pro-Phe-pNA (50 mM) in buffer containing 35 mM HEPES (pH 7.8), 0.2 mM DTT and 0.1 mg/ml BSA at 10°C as described previously⁶⁷. K_i value obtained from PPIase assay is derived from the Cheng-Prusoff equation [$K_i = IC_{50} / (1 + S/K_m)$], where K_m is the Michaelis constant for the used substrate, S is the initial concentration of the substrate in the assay, and the IC_{50} value of the inhibitor, as described⁶⁷. ATRA (R2625), Cyclosporin A (300224), and FK-506 (F4679) were all from Sigma.

Thermal shift assay

Two micrograms of recombinant PIN1 (VWR) was combined with EGCG, oxfendazole, buparvaquone, and nocodazole at 100 μ M and Protein Thermal Shift Buffer (Applied Biosciences). Mixtures were incubated at room temperature for 20 minutes, combined with Thermal Shift dye and subjected to differential scanning fluorimetry⁶⁸. Melt reactions from 20–90°C in 1.0°C increments were performed using a StepOne Plus instrument (Applied Biosciences). Fluorescence readings were acquired with excitation and emission

wavelengths of 580 ± 10 nm and 621 ± 14 nm, respectively. StepOne Plus Protein Thermal Shift Software (Applied Biosciences) was used to determine the T_m from each fluorescence profile and the T_m of a first derivative of the fluorescence data at each temperature was used to calculate T_m values.

Quantification of synergistic drug interactions

The synergy experiments were performed in both cell culture AlamarBlue survival and zebrafish dorsal tail curvature assays as described above. Subtherapeutic doses were chosen based on dose-response curves with the highest possible dose which produced <10% decrease in cell viability or <20% dorsal tail curves after IR in cell culture and zebrafish assays, respectively. This established our maximum tolerated dose (MTD). We then chose a dose at a five-fold decrease from the MTD and used both doses for synergy experiments, with one IRAK1 inhibitor and one PIN1 inhibitor. The analysis of synergy was done by the isobologram and combination-index methods, derived from the Chou-Talalay median-effect principle using CompuSyn software⁶⁹.

Clinical samples

Pre-treatment HNSCC tumors were examined. All patients were treated with a complete surgical resection followed by post-operative RT at MDACC. Tumor characteristics are shown in Supplementary Table 3. All studies involving human samples were approved by the MD Anderson Cancer Center Institutional Review Board in accordance with appropriate ethical regulations regarding research involving patient samples. Patient samples were collected as part of clinical protocols with appropriate consent. A total of 72 p16 negative tumors were analyzed for which both p53 status and IRAK1 and PIN1 expression was available. Ion torrent sequencing was performed as described previously to examine *TP53* status⁴⁴. mRNA expression was examined using Illumina HumanWG-6 V3 BeadChip human whole-genome expression arrays as described previously⁴⁴. For outcomes analysis, patients were first placed into two groups (36 in each group) by expression of either IRAK1, IRAK4, TRAF6 or PIN1 (high vs. low) and then further classified by *TP53* status (wild type vs. mutant). Multivariate analysis of clinical (tumor stage, nodal stage and tumor site) and mRNA-based (IRAK1, IRAK4, TRAF6 and PIN1) variables potentially affecting locoregional recurrence (LRR) was performed using forward stepwise Cox regression for the entire population as well as for the *TP53* mutant patients only. Kaplan Meier curves expressing LRR, time to distant metastasis (DM), disease free survival (DFS), and overall survival (OS) were generated and log rank statistics were used to determine significance between groups. R software, SPSS statistical software (v.20), and GraphPad Prism were used. On multivariate analysis for the entire patient population, no clinical characteristic or gene examined was associated with LRR following radiation. However, when LRR was examined in only those patients whose tumors harbor a *TP53* mutation, Nodal stage trended toward ($p=0.057$) and PIN1 expression was significantly ($p=0.018$) associated with LRR. Indeed, 64% of patients with a mutation in *TP53* and high levels of PIN1 had a LRR at 5 years, compared to around 25% for patients in all other groups (see Figure 6g, $p=0.006$).

Xenograft studies

NSG mice (Jackson Laboratories) were used for *in vivo* studies and were cared for in accordance with guidelines approved by the Memorial Sloan-Kettering Cancer Center Institutional Animal Care and Use Committee and Research Animal Resource Center. The study is compliant with all relevant ethical regulations regarding mouse research. 6–8 week old female mice were injected subcutaneously with 2 million SAS cells together with Matrigel⁷⁰. Once tumors reached an average volume of 100 mm³ (i.e., 6 days post-implantation), mice were randomized into four treatment groups: 1. Control (saline); 2. Localized radiation; 3. Ginsenoside Rb1 + EGCG; 4. Radiation + Ginsenoside Rb1 + EGCG. Dosing schedule was as follows: Ginsenoside Rb1 20 mg/kg i.p daily x 5 for 3 weeks, EGCG 50 mg/kg i.p QD3 for 3 weeks, localized radiation: 2.5 Gy once on day 1. For the drug/RT combination arm, RT was delivered 30 min after dosing the mice with Ginsenoside Rb1+EGCG. Mice were observed daily throughout the treatment period for signs of morbidity/mortality. Tumors were measured twice weekly using calipers, and volume was calculated using the formula: length x width² x 0.52. Body weight was also assessed twice weekly. After 3 weeks of treatment tumor samples were collected for immunoblot and HIC analysis.

Stainings of xenograft sections

For IF stainings, paraffin-embedded sections were de-paraffinized, followed by rehydration and antigen retrieval as described below. Paraffin-embedded tissue sections were kept at 60 degree Celsius in the oven for 15 minutes, followed by slide hydration in xylene and a graded alcohol series. For antigen retrieval, heat-induced epitope retrieval was performed using a vegetable steamer by incubating slides in 10 mM citrate buffer for 40 min at 60°C, followed by a wash in H₂O and PBS. Post washes, cell membranes were permeabilized in 0.1% Triton X-100 in PBS for 5 minutes at room temperature. For primary antibody staining, sections were blocked with 50mM NH₄Cl for 15 min at room temperature, followed by blocking with 3% normal goat serum (NGS) and 3% Bovine Serum Albumin (BSA) in PBS for 60 min at room temperature. Binding of the primary antibodies against Cleaved Caspase-3 (Asp175) rabbit antibody (Cell Signaling, catalog no. #9661) and Vimentin rat antibody (R&D systems, catalog no. MAB2105) was carried out at 4°C overnight, followed by PBS (2 x 5 min) washes. Prior to secondary antibody staining, sections were incubated with 3% normal goat serum (NGS) and 3% Bovine Serum Albumin (BSA) in PBS for 30 min at room temperature. Detection by secondary antibodies -Alexa Fluor 488 goat anti-rabbit (Invitrogen, catalog no. A11008) and Alexa Fluor 568 goat anti-rat (Invitrogen, catalog no. A11077) and was carried out at room temperature for 1 h in the dark. Slides were mounted in Vectashield with DAPI (Vector Laboratories, catalog no. CB-2000), following PBS (3 x 5 min) washes. The IF stainings were evaluated using a Leica TCS SP5 II confocal Laser-microscope with DAPI, GFP and RFP filters. 2 sections of each treated tumor and 3 fields of each tumor section were imaged at 60X magnification. For Hematoxylin and Eosin stainings, images were acquired using a Leica bright field microscope at a magnification of 40X.

Image analysis using Fiji software

Images were analyzed using the open-source processing software Fiji (ImageJ). Vimentin positive cells were scored for positive cleaved caspase-3 staining. For scoring caspase-3 positive cells, images of samples incubated with secondary antibody, but no primary antibody were used as background. The brightness and contrast of images was adjusted relative to primary antibody control stainings, to identify caspase-3 positive cells in all treated conditions. For this analysis, 3 fields of each tumor section and a total of 12 images, comprising of 4 tumor samples for each treated condition were analyzed. Total cell numbers per image were counted and the percentages of caspase-3 positive vimentin cells were calculated. Graphs were plotted using Excel and p values were calculated using t-test.

Statistics and Reproducibility

With the exception of TCGA and MDACC patient cohort studies (see TCGA Analysis and MDACC Clinical Samples sections above), paired two-tailed Students t-tests were used to determine p-values ($\alpha = 0.05$). The log rank test was used to determine p-values for survival curves. Data in bar graphs are represented as mean \pm SD or \pm SEM, as indicated in legends, and statistical significance was expressed as follows: *, $P < 0.05$; **, $P < 0.005$; ***, $P < 0.0005$; NS, not significant. Embryos from WT or *p53^{MK/MK}* zebrafish group matings were randomly allocated into experimental groups for irradiation, injections and/or drug treatments. Most experiments were carried out at least twice, and the findings of all key experiments were reliably reproduced. All replicates and precise *P* values are documented in Supplementary Table 4, which states the number of independent samples, embryos and independent experiments.

Supplementary Material

Refer to Web version on PubMed Central for supplementary material.

Acknowledgements:

We thank Eduardo Farias, Ross Cagan, Arvin Dar, Robert Krauss, Jonathan Ashwell, Xiaoxiao Li, Marshall Posner, Premkumar Reddy, Robert De Vita and Roberto Sanchez for helpful comments, technical advice and reagents, and Carlos Franco and Diarles Dominguez for zebrafish care. This work was supported in part by NIH/NCI F30CA186448 (P.H.L.), National Cancer Center NCC CCP postdoctoral fellowship (Y.L.), NIH/NCI P30 CA008748 (K.S.P.), NIH/NCI RO1CA168485 (H.D.S., J.V.H), and NIH/NCI RO1CA178162, JJR Foundation, Pershing Square Sohn Cancer Research Alliance, New York Community Trust and the Searle Scholars Program (S.S.).

References:

1. Lawrence YR, et al. NCI-RTOG translational program strategic guidelines for the early-stage development of radiosensitizers. *J Natl Cancer Inst* 105, 11–24 (2013). [PubMed: 23231975]
2. Sharma RA, et al. Clinical development of new drug-radiotherapy combinations. *Nat Rev Clin Oncol* 13, 627–642 (2016). [PubMed: 27245279]
3. Wilson GD, Bentzen SM & Harari PM Biologic basis for combining drugs with radiation. *Semin Radiat Oncol* 16, 2–9 (2006). [PubMed: 16378901]
4. Golden EB, Formenti SC & Schiff PB Taxanes as radiosensitizers. *Anticancer Drugs* 25, 502–511 (2014). [PubMed: 24335716]

5. Adelstein DJ, et al. An intergroup phase III comparison of standard radiation therapy and two schedules of concurrent chemoradiotherapy in patients with unresectable squamous cell head and neck cancer. *J Clin Oncol* 21, 92–98 (2003). [PubMed: 12506176]
6. Olivier M, et al. The IARC TP53 database: new online mutation analysis and recommendations to users. *Hum Mutat* 19, 607–614 (2002). [PubMed: 12007217]
7. Igney FH & Krammer PH Death and anti-death: tumour resistance to apoptosis. *Nat Rev Cancer* 2, 277–288 (2002). [PubMed: 12001989]
8. Vogelstein B, Lane D & Levine AJ Surfing the p53 network. *Nature* 408, 307–310 (2000). [PubMed: 11099028]
9. Vousden KH & Lu X Live or let die: the cell's response to p53. *Nat Rev Cancer* 2, 594–604 (2002). [PubMed: 12154352]
10. Poeta ML, et al. TP53 mutations and survival in squamous-cell carcinoma of the head and neck. *N Engl J Med* 357, 2552–2561 (2007). [PubMed: 18094376]
11. Skinner HD, et al. TP53 disruptive mutations lead to head and neck cancer treatment failure through inhibition of radiation-induced senescence. *Clin Cancer Res* 18, 290–300 (2012). [PubMed: 22090360]
12. Nam TK, et al. Molecular prognostic factors in rectal cancer treated by preoperative chemoradiotherapy. *Oncol Lett* 1, 23–29 (2010). [PubMed: 22966250]
13. Sclafani F, et al. TP53 mutational status and cetuximab benefit in rectal cancer: 5-year results of the EXPERT-C trial. *J Natl Cancer Inst* 106(2014).
14. Eikesdal HP, Knappskog S, Aas T & Lonning PE TP53 status predicts long-term survival in locally advanced breast cancer after primary chemotherapy. *Acta Oncol* 53, 1347–1355 (2014). [PubMed: 24909504]
15. Li S, Zhang W, Chen B, Jiang T & Wang Z Prognostic and predictive value of p53 in low MGMT expressing glioblastoma treated with surgery, radiation and adjuvant temozolomide chemotherapy. *Neurol Res* 32, 690–694 (2010). [PubMed: 19703338]
16. Tabori U, et al. Universal poor survival in children with medulloblastoma harboring somatic TP53 mutations. *J Clin Oncol* 28, 1345–1350 (2010). [PubMed: 20142599]
17. Berghmans S, et al. tp53 mutant zebrafish develop malignant peripheral nerve sheath tumors. *Proc Natl Acad Sci U S A* 102, 407–412 (2005). [PubMed: 15630097]
18. Sidi S, et al. Chk1 suppresses a caspase-2 apoptotic response to DNA damage that bypasses p53, Bcl-2, and caspase-3. *Cell* 133, 864–877 (2008). [PubMed: 18510930]
19. McAleer MF, et al. Novel use of zebrafish as a vertebrate model to screen radiation protectors and sensitizers. *Int J Radiat Oncol Biol Phys* 61, 10–13 (2005). [PubMed: 15629588]
20. Lacey E Mode of action of benzimidazoles. *Parasitol Today* 6, 112–115 (1990). [PubMed: 15463312]
21. Prichard RK & Ranjan S Anthelmintics. *Vet Parasitol* 46, 113–120 (1993). [PubMed: 8484204]
22. Keiser MJ, et al. Relating protein pharmacology by ligand chemistry. *Nat Biotechnol* 25, 197–206 (2007). [PubMed: 17287757]
23. Jain A, Kaczanowska S & Davila E IL-1 Receptor-Associated Kinase Signaling and Its Role in Inflammation, Cancer Progression, and Therapy Resistance. *Front Immunol* 5, 553 (2014). [PubMed: 25452754]
24. Janssens S & Beyaert R Functional diversity and regulation of different interleukin-1 receptor-associated kinase (IRAK) family members. *Mol Cell* 11, 293–302 (2003). [PubMed: 12620219]
25. Powers JP, et al. Discovery and initial SAR of inhibitors of interleukin-1 receptor-associated kinase-4. *Bioorg Med Chem Lett* 16, 2842–2845 (2006). [PubMed: 16563752]
26. Wang Z, et al. Crystal structures of IRAK-4 kinase in complex with inhibitors: a serine/threonine kinase with tyrosine as a gatekeeper. *Structure* 14, 1835–1844 (2006). [PubMed: 17161373]
27. O' Neill LA, Golenbock D & Bowie AG The history of Toll-like receptors - redefining innate immunity. *Nat Rev Immunol* 13, 453–460 (2013). [PubMed: 23681101]
28. Rolf MG, et al. In vitro pharmacological profiling of R406 identifies molecular targets underlying the clinical effects of fostamatinib. *Pharmacol Res Perspect* 3, e00175 (2015). [PubMed: 26516587]

29. Joh EH, Lee IA, Jung IH & Kim DH Ginsenoside Rb1 and its metabolite compound K inhibit IRAK-1 activation--the key step of inflammation. *Biochem Pharmacol* 82, 278–286 (2011). [PubMed: 21600888]
30. Yao J, et al. Interleukin-1 (IL-1)-induced TAK1-dependent Versus MEKK3-dependent NFkappaB activation pathways bifurcate at IL-1 receptor-associated kinase modification. *J Biol Chem* 282, 6075–6089 (2007). [PubMed: 17197697]
31. Kollewe C, et al. Sequential autophosphorylation steps in the interleukin-1 receptor-associated kinase-1 regulate its availability as an adapter in interleukin-1 signaling. *J Biol Chem* 279, 5227–5236 (2004). [PubMed: 14625308]
32. Wee ZN, et al. IRAK1 is a therapeutic target that drives breast cancer metastasis and resistance to paclitaxel. *Nat Commun* 6, 8746 (2015). [PubMed: 26503059]
33. Muroi M & Tanamoto K IRAK-1-mediated negative regulation of Toll-like receptor signaling through proteasome-dependent downregulation of TRAF6. *Biochim Biophys Acta* 1823, 255–263 (2012). [PubMed: 22033459]
34. Rhyasen GW & Starczynowski DT IRAK signalling in cancer. *Br J Cancer* 112, 232–237 (2015). [PubMed: 25290089]
35. Conze DB, Wu CJ, Thomas JA, Landstrom A & Ashwell JD Lys63-linked polyubiquitination of IRAK-1 is required for interleukin-1 receptor- and toll-like receptor-mediated NF-kappaB activation. *Mol Cell Biol* 28, 3538–3547 (2008). [PubMed: 18347055]
36. Ando K, et al. PIDD death-domain phosphorylation by ATM controls prodeath versus prosurvival PIDDosome signaling. *Mol Cell* 47, 681–693 (2012). [PubMed: 22854598]
37. Sladky V, Schuler F, Fava LL & Villunger A The resurrection of the PIDDosome - emerging roles in the DNA-damage response and centrosome surveillance. *J Cell Sci* 130, 3779–3787 (2017). [PubMed: 29142064]
38. Tinel A & Tschopp J The PIDDosome, a protein complex implicated in activation of caspase-2 in response to genotoxic stress. *Science* 304, 843–846 (2004). [PubMed: 15073321]
39. Tinel A, et al. Autoproteolysis of PIDD marks the bifurcation between pro-death caspase-2 and pro-survival NF-kappaB pathway. *EMBO J* 26, 197–208 (2007). [PubMed: 17159900]
40. Barretina J, et al. The Cancer Cell Line Encyclopedia enables predictive modelling of anticancer drug sensitivity. *Nature* 483, 603–607 (2012). [PubMed: 22460905]
41. Essmann F, Engels IH, Totzke G, Schulze-Osthoff K & Janicke RU Apoptosis resistance of MCF-7 breast carcinoma cells to ionizing radiation is independent of p53 and cell cycle control but caused by the lack of caspase-3 and a caffeine-inhibitable event. *Cancer Res* 64, 7065–7072 (2004). [PubMed: 15466201]
42. Lu Z & Hunter T Prolyl isomerase Pin1 in cancer. *Cell Res* 24, 1033–1049.
43. Wei S, et al. Active Pin1 is a key target of all-trans retinoic acid in acute promyelocytic leukemia and breast cancer. *Nat Med* 21, 457–466 (2015). [PubMed: 25849135]
44. Skinner HD, et al. Proteomic Profiling Identifies PTK2/FAK as a Driver of Radioresistance in HPV-negative Head and Neck Cancer. *Clin Cancer Res* 22, 4643–4650 (2016). [PubMed: 27036135]
45. Cancer Genome Atlas N Comprehensive genomic characterization of head and neck squamous cell carcinomas. *Nature* 517, 576–582 (2015). [PubMed: 25631445]
46. Tun-Kyi A, et al. Essential role for the prolyl isomerase Pin1 in Toll-like receptor signaling and type I interferon-mediated immunity. *Nat Immunol* 12, 733–741 (2011). [PubMed: 21743479]
47. Moore JD & Potter A Pin1 inhibitors: Pitfalls, progress and cellular pharmacology. *Bioorg Med Chem Lett* 23, 4283–4291. [PubMed: 23796453]
48. Urusova DV, et al. Epigallocatechin-gallate suppresses tumorigenesis by directly targeting Pin1. *Cancer Prev Res (Phila)* 4, 1366–1377.
49. Marsolier J, et al. Theileria parasites secrete a prolyl isomerase to maintain host leukocyte transformation. *Nature* 520, 378–382. [PubMed: 25624101]
50. Candeias SM & Testard I The many interactions between the innate immune system and the response to radiation. *Cancer Lett* 368, 173–178 (2015). [PubMed: 25681669]

51. Reisz JA, Bansal N, Qian J, Zhao W & Furdul CM Effects of ionizing radiation on biological molecules--mechanisms of damage and emerging methods of detection. *Antioxid Redox Signal* 21, 260–292 (2014). [PubMed: 24382094]
52. Thomas JA, et al. Impaired cytokine signaling in mice lacking the IL-1 receptor-associated kinase. *J Immunol* 163, 978–984 (1999). [PubMed: 10395695]
53. Liou YC, et al. Role of the prolyl isomerase Pin1 in protecting against age-dependent neurodegeneration. *Nature* 424, 556–561 (2003). [PubMed: 12891359]
54. Girardini JE, et al. A Pin1/mutant p53 axis promotes aggressiveness in breast cancer. *Cancer Cell* 20, 79–91 (2011). [PubMed: 21741598]
55. Anderson JR, Cain KC & Gelber RD Analysis of survival by tumor response. *J Clin Oncol* 1, 710–719 (1983). [PubMed: 6668489]
56. Braselmann S, et al. R406, an orally available spleen tyrosine kinase inhibitor blocks fc receptor signaling and reduces immune complex-mediated inflammation. *J Pharmacol Exp Ther* 319, 998–1008 (2006). [PubMed: 16946104]
57. Fujiki H, et al. Anticarcinogenic effects of (–)-epigallocatechin gallate. *Prev Med* 21, 503–509 (1992). [PubMed: 1409491]
58. Notredame C, Higgins DG & Heringa J T-Coffee: A novel method for fast and accurate multiple sequence alignment. *J Mol Biol* 302, 205–217 (2000). [PubMed: 10964570]
59. Sali A & Blundell TL Comparative protein modelling by satisfaction of spatial restraints. *J Mol Biol* 234, 779–815 (1993). [PubMed: 8254673]
60. Eramian D, Eswar N, Shen MY & Sali A How well can the accuracy of comparative protein structure models be predicted? *Protein Sci* 17, 1881–1893 (2008). [PubMed: 18832340]
61. Ung PM & Schlessinger A DFGmodel: predicting protein kinase structures in inactive states for structure-based discovery of type-II inhibitors. *ACS Chem Biol* 10, 269–278 (2015). [PubMed: 25420233]
62. Sherman W, Day T, Jacobson MP, Friesner RA & Farid R Novel procedure for modeling ligand/receptor induced fit effects. *J Med Chem* 49, 534–553 (2006). [PubMed: 16420040]
63. Ye H, et al. Distinct molecular mechanism for initiating TRAF6 signalling. *Nature* 418, 443–447 (2002). [PubMed: 12140561]
64. Langheinrich U, Hennen E, Stott G & Vacun G Zebrafish as a model organism for the identification and characterization of drugs and genes affecting p53 signaling. *Curr Biol* 12, 2023–2028 (2002). [PubMed: 12477391]
65. Thompson R, et al. An Inhibitor of PIDDosome Formation. *Mol Cell* 58, 767–779 (2015). [PubMed: 25936804]
66. Wei S, et al. Active Pin1 is a key target of all-trans retinoic acid in acute promyelocytic leukemia and breast cancer. *Nat Med* 21, 457–466. [PubMed: 25849135]
67. Yaffe MB, et al. Sequence-specific and phosphorylation-dependent proline isomerization: a potential mitotic regulatory mechanism. *Science* 278, 1957–1960 (1997). [PubMed: 9395400]
68. Niesen FH, Berglund H & Vedadi M The use of differential scanning fluorimetry to detect ligand interactions that promote protein stability. *Nat Protoc* 2, 2212–2221 (2007). [PubMed: 17853878]
69. Chou TC Theoretical basis, experimental design, and computerized simulation of synergism and antagonism in drug combination studies. *Pharmacol Rev* 58, 621–681 (2006). [PubMed: 16968952]
70. Kawata M, et al. Additive effect of radiosensitization by 2-deoxy-D-glucose delays DNA repair kinetics and suppresses cell proliferation in oral squamous cell carcinoma. *J Oral Pathol Med* 46, 979–985 (2017). [PubMed: 28640935]

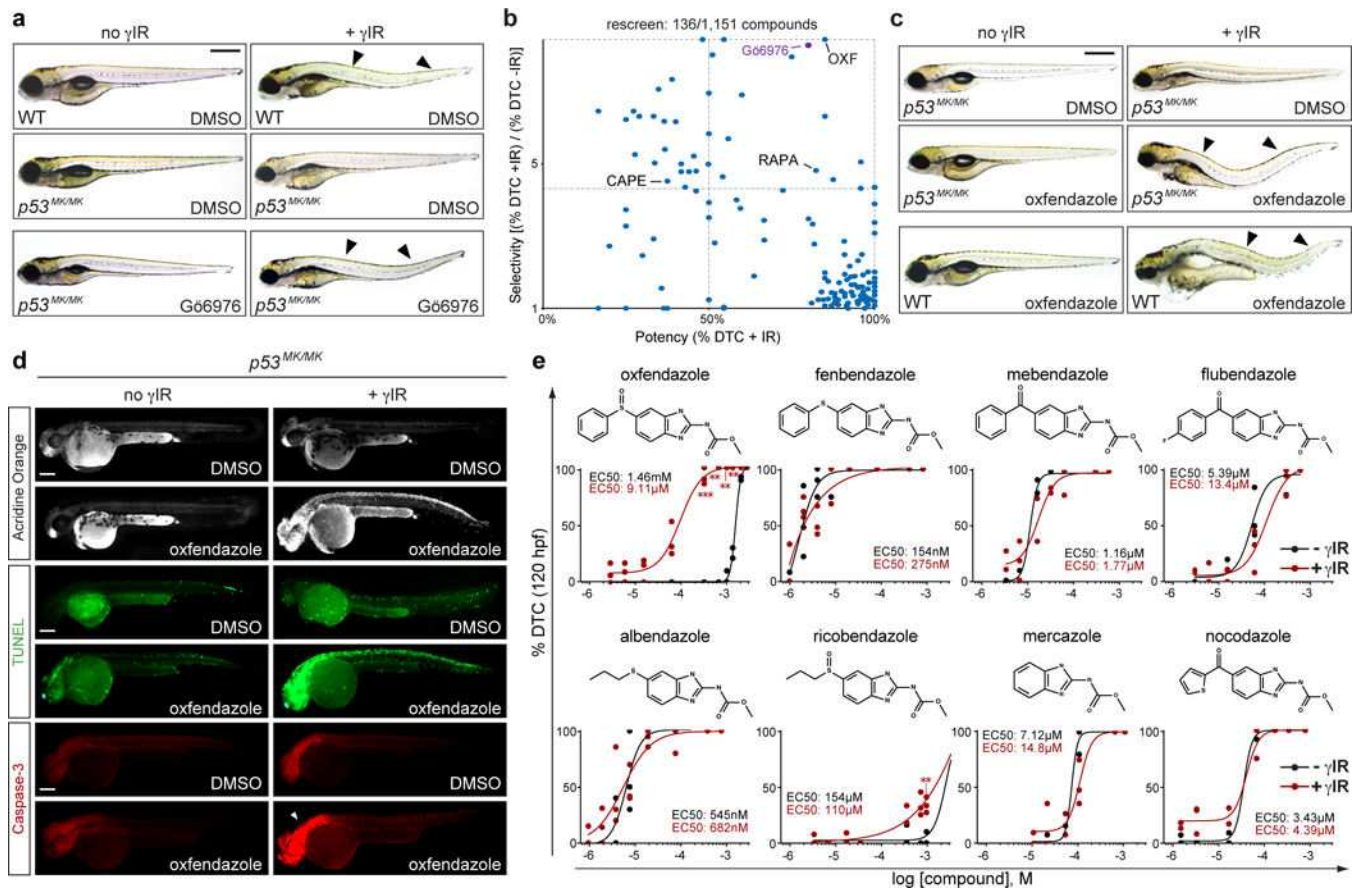


Fig. 1. *In vivo* zebrafish drug screen identifies ox fendazole as a radiosensitizer of *p53* mutant embryos.

(a) ^{37}Cs -irradiated *p53*^{M214K/M214K} (*p53*^{MK/MK}) zebrafish embryos (15 Gy TBI at 18 hpf) observed at 120 hpf lack the dorsal tail curvature (DTC) phenotype of wild-type (WT) embryos (arrowheads, a late readout of embryonic radiosensitivity). DTCs are restored with Chk1 inhibitor (Gö6976, 1 μM) in an average of 75% of mutants per experiment (see Supplemental Fig. 1d). hpf, hours post fertilization. DTC, dorsal tail curvature. TBI, total body irradiation. γIR , gamma-irradiation from ^{137}Cs source. (b) Re-screen of top 136 hits from primary screen (see Supplementary Fig. 1c-g), scored for potency (%DTC after γIR) and selectivity [(%DTC after γIR) / (%DTC without γIR)], identifying ox fendazole (OXF) as the top hit. Capecitabine (CAPE) and rapamycin (RAPA), two known clinical radiosensitizers, were also recovered in the blind screen, providing internal validation of DTC assay. (c) Doses of ox fendazole (shown here, 63 μM) that suppress R-RT in *p53*^{MK/MK} embryos are fully tolerated in the absence of γIR , including in WT animals. (d) *p53*^{MK/MK} mutants treated with ox fendazole+IR score positive for acridine orange (AO), a vital marker of cell death, and apoptosis markers (TUNEL, anti-active caspase-3) at 48hpf. (e) Structure-activity relationship (SAR) of benzimidazole tubulin-binding analogs in dose-response curves for 120 hpf *p53*^{MK/MK} embryos scored for DTCs. Chemical structure of each analog shown. Black curves, no IR. Red curves, 15 Gy TBI delivered at 18 hpf. Data shown as means of $n = 3$ independent experiments for ox fendazole-IR (10–40 μM), ox fendazole+IR (0.1–40 μM), flubendazole-IR (0.1–10 μM), flubendazole+IR (0.1–10 μM), albendazole-IR

(0.05–0.2 μM), albendazole+IR (0.05–2.0 μM), mebendazole-IR (0.2–2.0 μM), mebendazole +IR (0.1–2.0 μM), fenbendazole-IR (0.05–0.1 μM), fenbendazole+R (0.025–0.1 μM), ricobendazole-IR (20–75 μM), ricobendazole+IR (20–75 μM), mercazole-IR (2 μM), mercazole+IR (2 μM); and $n = 2$ independent experiments for the remaining data points, as indicated by the dot plots and as detailed in Supplementary Fig. 5, with >21 embryos scored per experiment; * $P < 0.05$, ** $P < 0.005$, *** $P < 0.0005$, two-tailed Student's t -test ($\alpha = 0.05$). See Supplementary Table 4 for statistics source data including precise P values. Scale bars, 0.5 (**a,c**) and 0.2 (**d**) mm.

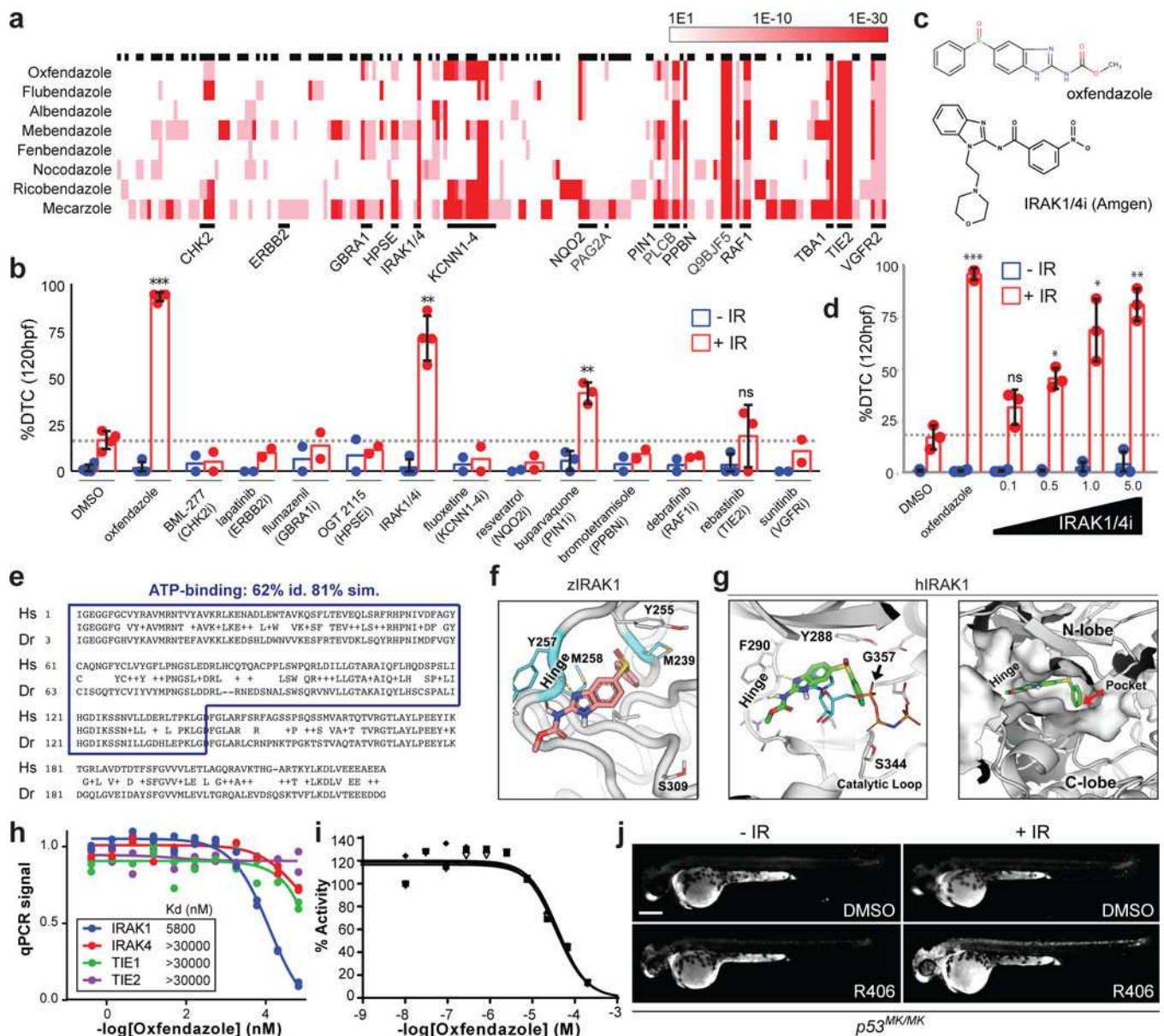


Fig. 2. Target discovery for ox fendazole identifies IRAK1.

(a) Similarity Ensemble Approach (SEA) predicted targets of ox fendazole and analogs. E-value color-coded white to red. Black bars, predicted targets for ox fendazole. (b) DTC assay of *p53^{MK/MK}* embryos (120 hpf) treated with inhibitors of SEA-predicted ox fendazole targets (see a) with or without 15 Gy γ IR (red and blue bars, respectively). Dotted line, penetrance cutoff at DMSO+IR levels. Data represented as means \pm SD of $n = 4$ independent experiments (DMSO, IRAK1/4i), $n = 3$ independent experiments (ox fendazole, buparvaquone, rebastinib) or $n = 2$ independent experiments (remaining drugs) with >12 embryos per experiment. Relative to DMSO-treated irradiated embryos (bar 2), ** $P < 0.005$, *** $P < 0.0005$, ns, not significant, two-tailed Student's t -test. (c) Chemical structures of indicated drugs. (d) Dose-response to IRAK1/4i of *p53^{MK/MK}* embryos scored in DTC assay. Data represented as means \pm SD of $n = 3$ independent experiments, * $P < 0.05$, ** P

< 0.005, *** $P < 0.0005$, n.s., not significant, relative to DMSO-treated irradiated embryos (bar 2), two-tailed Student's t -test. **(e)** Sequence alignment of human (Hs) and zebrafish (Dr) IRAK1 kinase domains, ATP binding domain boxed in blue. Id, identity, sim., similarity. **(f,g)** Induced-fit docking of oxfendazole to ATP-binding site of zebrafish **(f)** and human **(g)** IRAK1 models. Gate-keeper residue: Y255 (Y288 in human). 3 residue changes near proposed docking pose within binding site highlighted in cyan in zebrafish model: M239, Y257, and M258 (V272, F290 and L291 in human). **(h-i)** KINOMEScan *in vitro* kinase capture assay for indicated kinases **(h)** and *in vitro* kinase assay vs. IRAK1 **(i)**, curved-fit from 2 and 3 replicates, respectively. **(j)** IRAK1 inhibitor R406 (40 $\mu\text{g}/\text{ml}$) phenocopies oxfendazole (see **1d**) in AO assay at 48 hpf, with images representative of 2 independent experiments. See Supplementary Table 4 for statistics source data including precise P values. Scale bar, 0.2 mm.

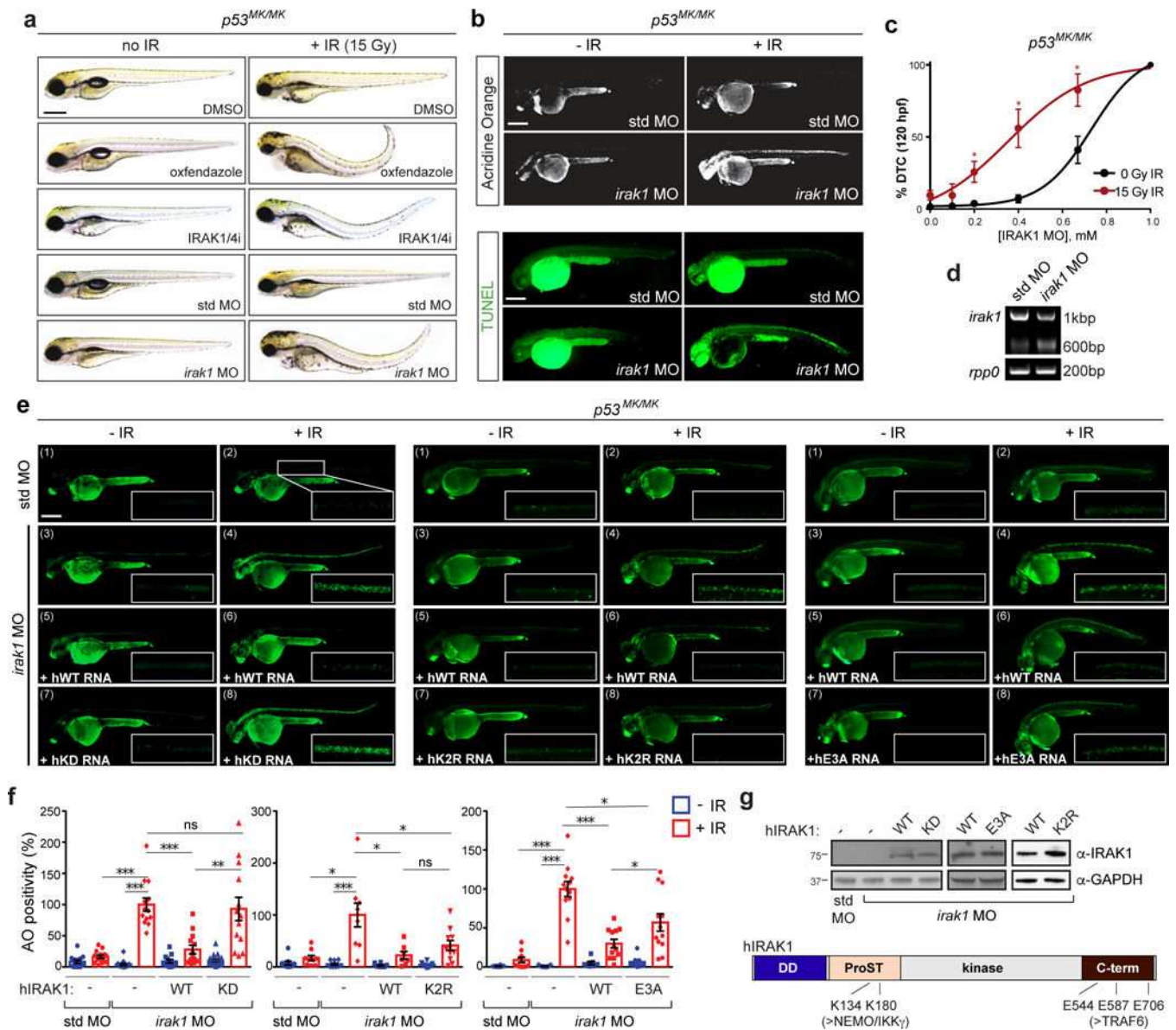


Fig. 3. Targeting *irak1* overcomes R-RT in $p53^{MK/MK}$ zebrafish.

(a-c) Morpholino (MO) depletion of Irak1 phenocopies oxfendazole and IRAK1/4 inhibitor (IRAK1/4i) in DTC (a), AO (b, top) and TUNEL (b, bottom) assays (oxfendazole shown in 1d). *std*, standard control. (c) MO dose response in $p53^{MK/MK}$ embryos in DTC assay. Data are means \pm SD of $n = 3$ independent experiments. (d) RT-PCR of pooled embryonic extracts showing reduced WT mRNA levels (upper band) and skipping of exon 4 (lower band). *rpp0*, ribosomal protein P0. (e-f) Representative images (e) and quantification (f) of *irak1*-depleted $p53^{MK/MK}$ embryos reconstituted with WT vs. KD (left), WT vs. K2R (middle) or WT vs. E3A (right) human IRAK1 (hIRAK1) mRNA scored in AO assay. KD, kinase dead; K2R; K134R/K180R; E3A, E544A/E706A/E587A. Number of quantified, independent images (as boxed in e): Left: *std* MO+mock: n of non-irradiated = 14, n of irradiated = 14; *irak1* MO+mock: n of non-irradiated = 13, n of irradiated = 13; *irak1* MO +WT: n of non-irradiated = 12, n of irradiated = 13; *irak1* MO+KD: n of non-irradiated = 15,

n of irradiated = 13; Middle: *std*MO+mock: *n* of non-irradiated = 9, *n* of irradiated = 9; *irak1* MO+mock: *n* of non-irradiated = 9, *n* of irradiated = 9; *irak1* MO+WT: *n* of non-irradiated = 8, *n* of irradiated = 7; *irak1* MO+KD: *n* of non-irradiated = 10, *n* of irradiated = 11; Right: *std*MO+mock: *n* of non-irradiated = 8, *n* of irradiated = 10; *irak1* MO+mock: *n* of non-irradiated = 7, *n* of irradiated = 12; *irak1* MO+WT: *n* of non-irradiated = 7, *n* of irradiated = 12; *irak1* MO+KD: *n* of non-irradiated = 8, *n* of irradiated = 12. Raw images of all embryos and cropped spinal chord areas available at [10.6084/m9.figshare.7427942](https://doi.org/10.6084/m9.figshare.7427942). (g) Western blot of embryonic extracts showing hIRAK1 levels and diagram of hIRAK1, with disrupted residues and interactions shown. All data represented as means \pm SD, * $P < 0.05$, ** $P < 0.005$, *** $P < 0.0005$, ns, not significant, two-tailed Student's *t*-test. See Supplementary Table 4 and Supplementary Fig. 8 for statistics source data including precise *P* values and unprocessed immunoblots, respectively. Scale bars, 0.5 (a) and 0.2 (b,e) mm.

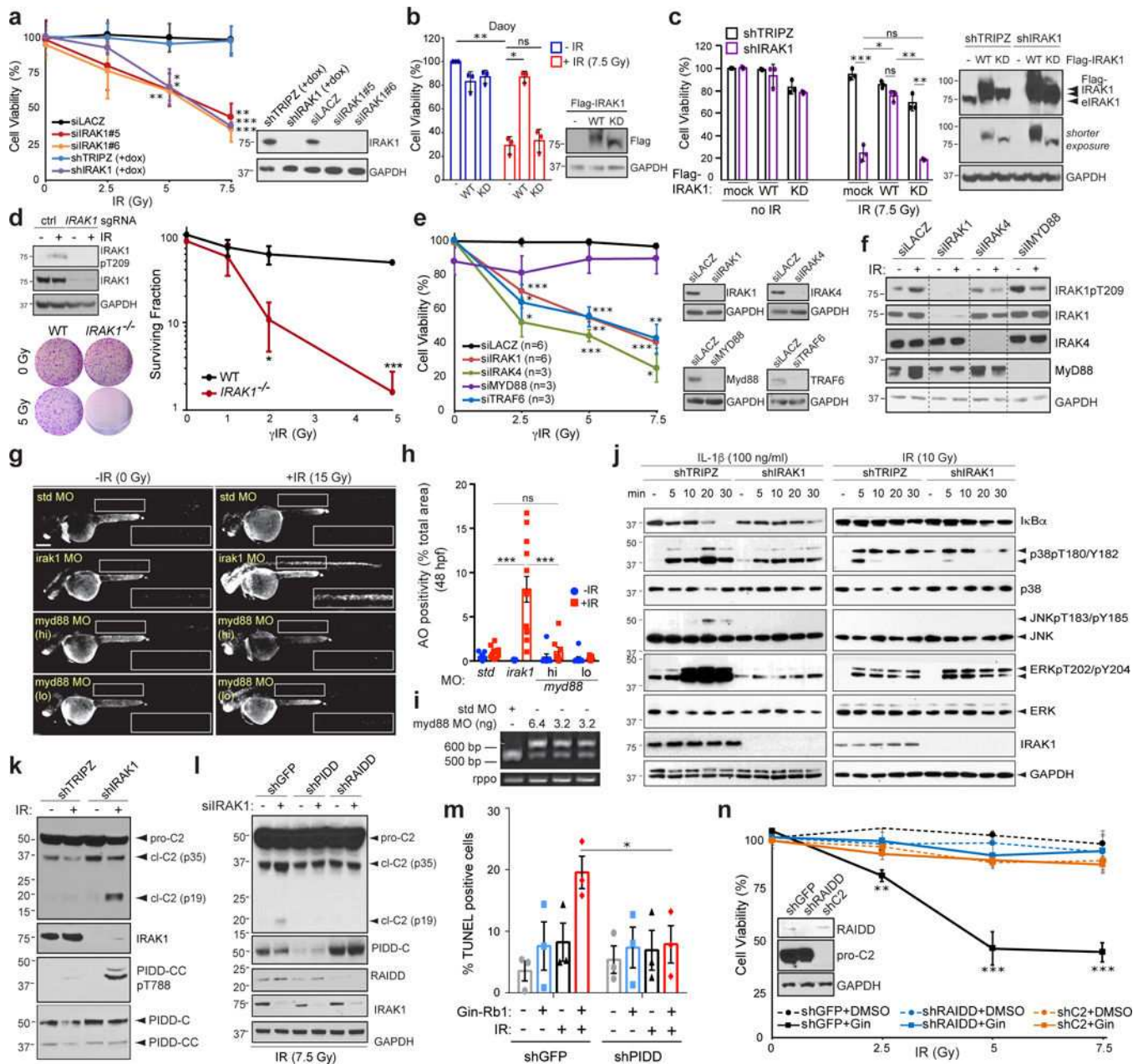


Fig. 4. IRAK1 acts independently of MyD88 and counters PIDDosome signalling. (a-f, j-n) HeLa (a,d-f,j-n), Daoy (b) and CAL27 (c) cells transfected with indicated siRNA (a,e-f), WT or kinase dead (KD) Flag-IRAK1 (b-c), *IRAK1* sgRNA plus Cas9 plasmid (d), and/or stably expressing indicated dox-inducible shRNA (a,c,k) or non-inducible shRNA (l-n), and/or treated with IRAK1 inhibitor Gin-Rb1 (10 μ g/ml) (m,n) were analyzed 5 days post IR (dpIR, IR doses in Gy) by alamarBlue cell viability assay (a-c,e,n), 14 dpIR by clonogenic assay (d), 2dpIR by TUNEL assay (m), and/or by western blot with indicated antibodies (a-f, j-l) at indicated minutes post-IR or interleukin 1 β (IL-1 β) treatment (j) or 24 hpIR (a-f, k-l, n). eIRAK1 (in c), endogenous IRAK1. In (k-l, n), pro-C2, procaspase-2; cl-C2 (p35), intermediate cleavage product; cl-C2 (p19), mature cleavage product. Data in a-e

and **m-n** represent means \pm SD, $n = 3$ independent experiments performed in triplicates. In **j**, activation of the following pathways marked by: gradual decline in I κ B levels (NF- κ B); p38 T180/Y182 phosphorylation (p38/MAPK); JNK T183/Y185 phosphorylation (JNK); ERK T202/Y204 phosphorylation (ERK). (**g-h**) Representative images (as in **3b** for *std* and *irak1* MOs) and quantification of *p53*^{MK/MK} embryos injected with indicated MOs and treated with or without 15 Gy IR at 18 hpf (blue and red bars in **h**, respectively) analyzed in AO assay at 24 hpIR. Number of quantified spinal chord images (as boxed in **g**) from 4 independent experiments (bars 1–4) or 3 independent experiments (bars 5–8) were: *std* MO: n of non-irradiated = 9, n of irradiated = 11; *irak1* MO: n of non-irradiated = 11, n of irradiated = 13; *myd88* MO high (hi, 6.4 ng): n of non-irradiated = 7, n of irradiated = 8; *myd88* MO low (lo, 3.2 ng): n of non-irradiated = 9, n of irradiated = 11. (**i**) RT-PCR of pooled embryo mRNA extracts shows MO dose-dependent intron retention in *myd88* message. * $P < 0.05$, ** $P < 0.005$, *** $P < 0.0005$ throughout the figure, n.s., not significant, two-tailed Student's t -test. See Supplementary Table 4 and Supplementary Fig. 8 for statistics source data including precise P values and unprocessed immunoblots, respectively. Scale bar, 0.2 mm.

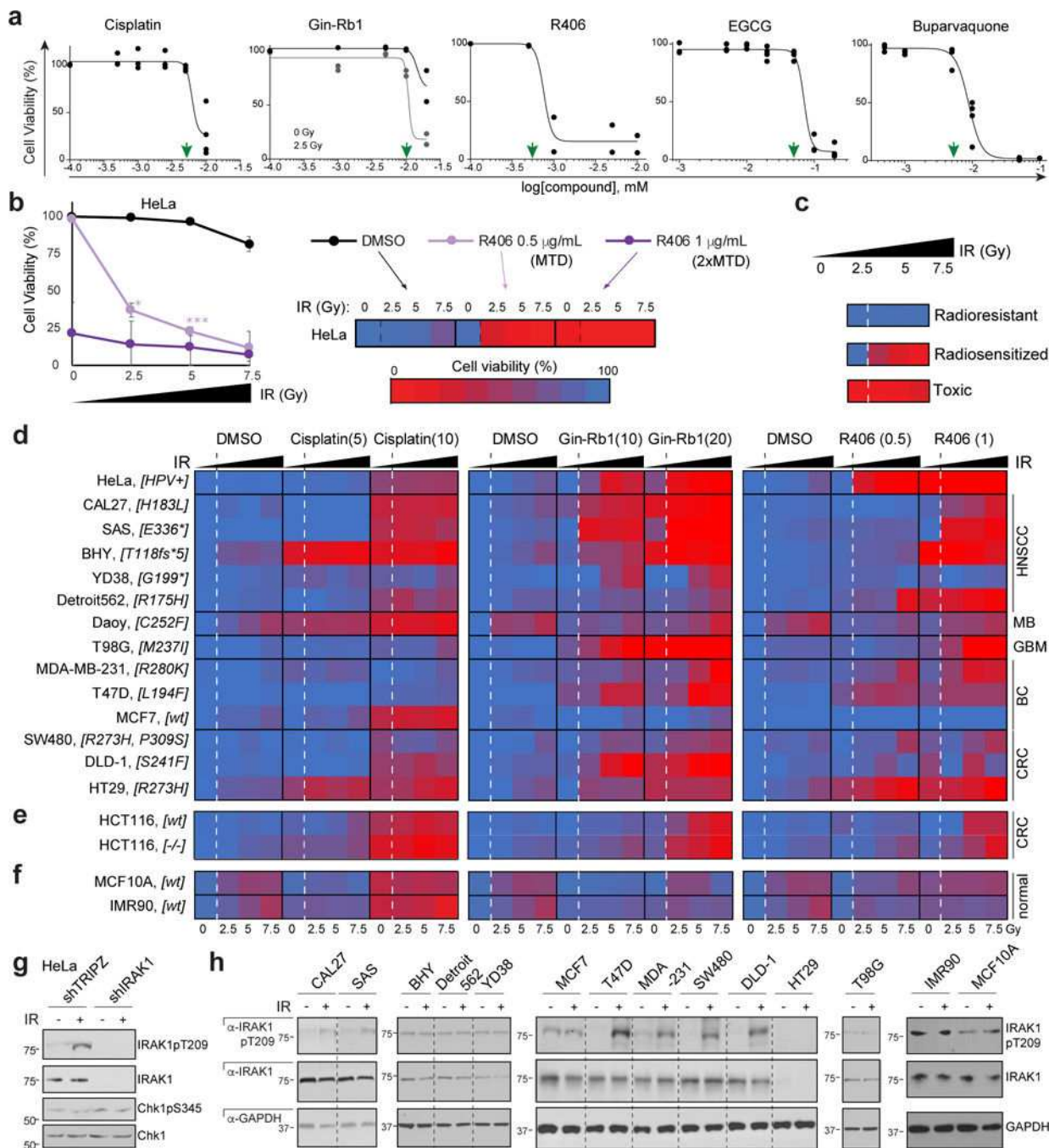


Fig. 5. IRAK1 inhibitors restore radiosensitivity across *TP53* mutant tumour cell models.

(a) AlamarBlue-based HeLa cell viability assays establish MTDs (green arrowheads) for cisplatin, IRAK1 inhibitors Ginsenoside-Rb1 (Gin-Rb1) and R406, and PIN1 inhibitors EGCG and buparvaquone. Gin-Rb1 required 2.5 Gy to achieve MTD at doses below the precipitation point of the drug. $n = 2$ independent experiments in triplicates, data represented as means. (b-c) Explanatory schematic for heatmap shown in (d), with R406 on IR-treated HeLa cells as example. (b) Cells treated with MTD (0.5 µg/mL) and 2xMTD (1 µg/mL) with 3 doses of IR represented in a standard dose-response curve (left) and corresponding heatmap.

map representation (right). Cell viability color code shown from red at 0% to blue at 100%. Note that this example showcases the three main phenotypic classes observed in the screen shown in **(d)**: ‘radioresistant’, ‘radiosensitized’, and ‘toxic’ (individually depicted in **(a)**). Data represented as means of $n = 3$ independent experiments, $P < 0.05$, $**P < 0.005$, $***P < 0.0005$, two-tailed Student’s t -test. Source data available in supplementary Table 4, sheet S5. **(d-f)** AlamarBlue-based cell viability heatmaps of radioresistant cancer cell lines (**d**, cell line names indicated to the left with *TP53* genotype in brackets and tumor of origin to the right), WT and *TP53* null HCT116 cells (**e**) and normal human cells (MCF10A, IMR90, **f**) treated with cisplatin or IRAK1 inhibitors, Gin-Rb1 and R406, at indicated doses (MTD and 2xMTD, $\mu\text{g/ml}$) and IR (0, 2.5, 5 and 7.5 Gy, as indicated) in $n = 3$ independent experiments performed in triplicates. Corresponding survival curves and P values shown in Supplementary Fig. 5. **(g)** Indicated HeLa shRNA lines treated with or without IR (10 Gy) and analyzed by western blot at 24 hpIR. **(f)** Cell lines as in **d** treated with or without IR (10 Gy) and analyzed by western blot 24 hpIR. 7 of 9 lines reliably radiosensitized by IRAK1 inhibitors (HeLa, CAL27, SAS, T47D, MDA-MB-231, SW480 and DLD-1, see **d**) engage IRAK1 phosphorylation in response to IR while both resistant lines (BHY, MCF7) do not. See Supplementary Table 4 and Supplementary Fig. 8 for statistics source data including precise P values and unprocessed immunoblots, respectively.

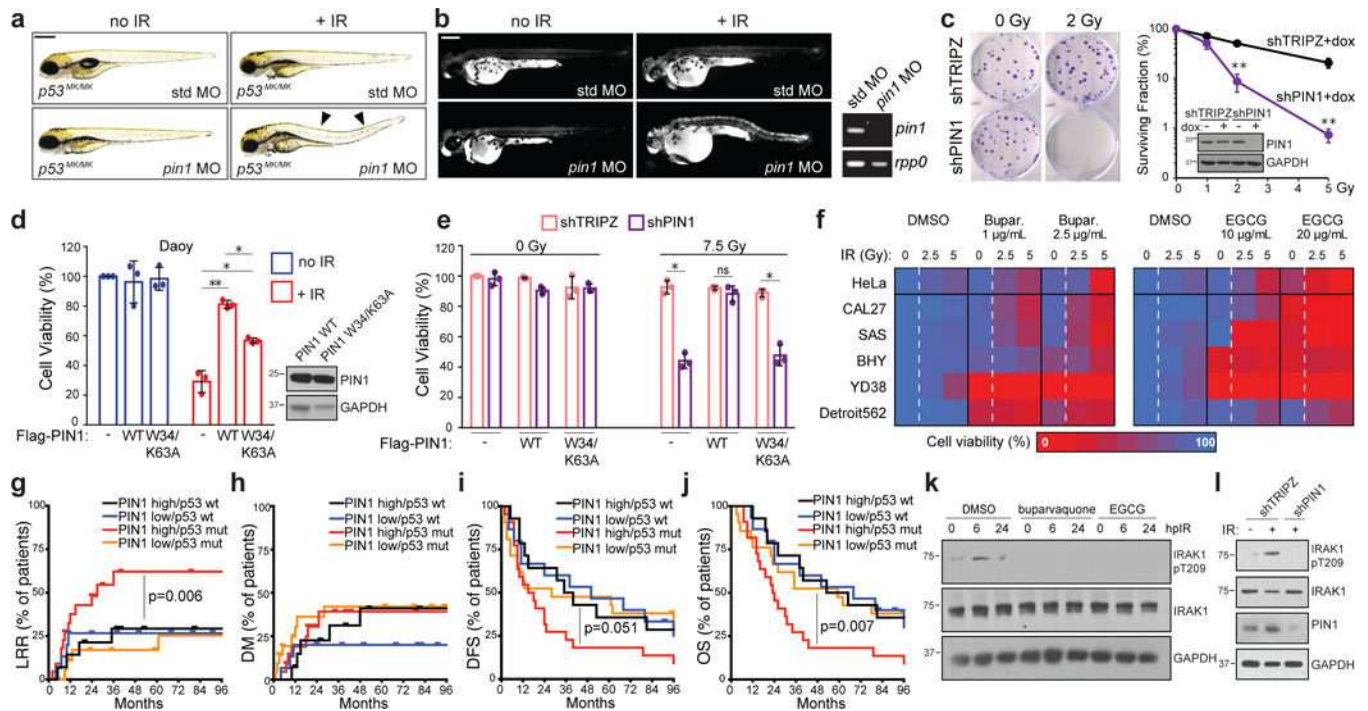


Fig. 6. PIN1 inhibition overcomes R-RT in zebrafish and human tumour-cell models while its overexpression associates with *TP53* mutant HNSCC recurrence. (a-b) MO depletion of Pin1 but not std MO restores DTCs (a) and AO uptake (b) after 15 Gy IR. See Supplementary Fig. 6c-d for quantifications. (b, right) RT-PCR of embryonic mRNA extracts detect nonsense mediated decay of *pin1* mRNA. (c) Clonogenic assay of shTRIPZ and shPIN1 HeLa cells after up to 5 Gy IR. Surviving fractions to the right. Western blot showing PIN1 knockdown also shown. (d) Daoy cells transfected with mock, WT or catalytically inactive (W34/K63A) PIN1, exposed to 0 or 7.5 Gy IR and assayed by alamarBlue at 5dpIR. Western blot of Flag-PIN1 levels also shown. (e) shTRIPZ and shPIN1 CAL27 cells reconstituted with Flag-PIN1 constructs exposed to 0 or 7.5 Gy IR and assayed by alamarBlue at 5 dpIR. Data in (c-e) are means \pm SD of $n = 3$ independent experiments performed in triplicates. * $P < 0.05$, ** $P < 0.005$, two-tailed Student's t -test. (f) MTD and 2xMTD of buparvaquone and EGCG given to indicated cell lines with 0, 2.5 or 5 Gy IR and analyzed by alamarBlue in $n = 3$ independent experiments in triplicates. Color coding as in Fig. 5d. Corresponding survival curves including p-values shown in Supplementary Fig. 6n. (g-j) Kaplan-Meier curves showing LRR (locoregional recurrence, g), DM (distant metastases, h), DFS (disease-free survival, i) and OS (overall survival, j) in patients from the MDACC HNSCC cohort split at median PIN1 expression and analyzed by two sided log-rank test. All patients treated with complete surgical resection followed by post-operative RT. n of patients with: PIN1^{high}/*TP53* WT = 14; PIN1^{low}/*TP53* WT = 15; PIN1^{high}/*TP53* MUT = 22; PIN1^{low}/*TP53* MUT = 21. See Supplemental Table 3 for patient characteristics. (k-l) HeLa cells treated with buparvaquone (1 μ g/ml) or EGCG (10 μ g/ml) (k) or stably expressing indicated shRNAs (l), treated with 0 or 10 Gy IR and analyzed by western blot at indicated hours post IR (hpIR). See Supplementary Table 4 and Supplementary Fig. 8 for statistics source data including precise P values and unprocessed immunoblots, respectively.

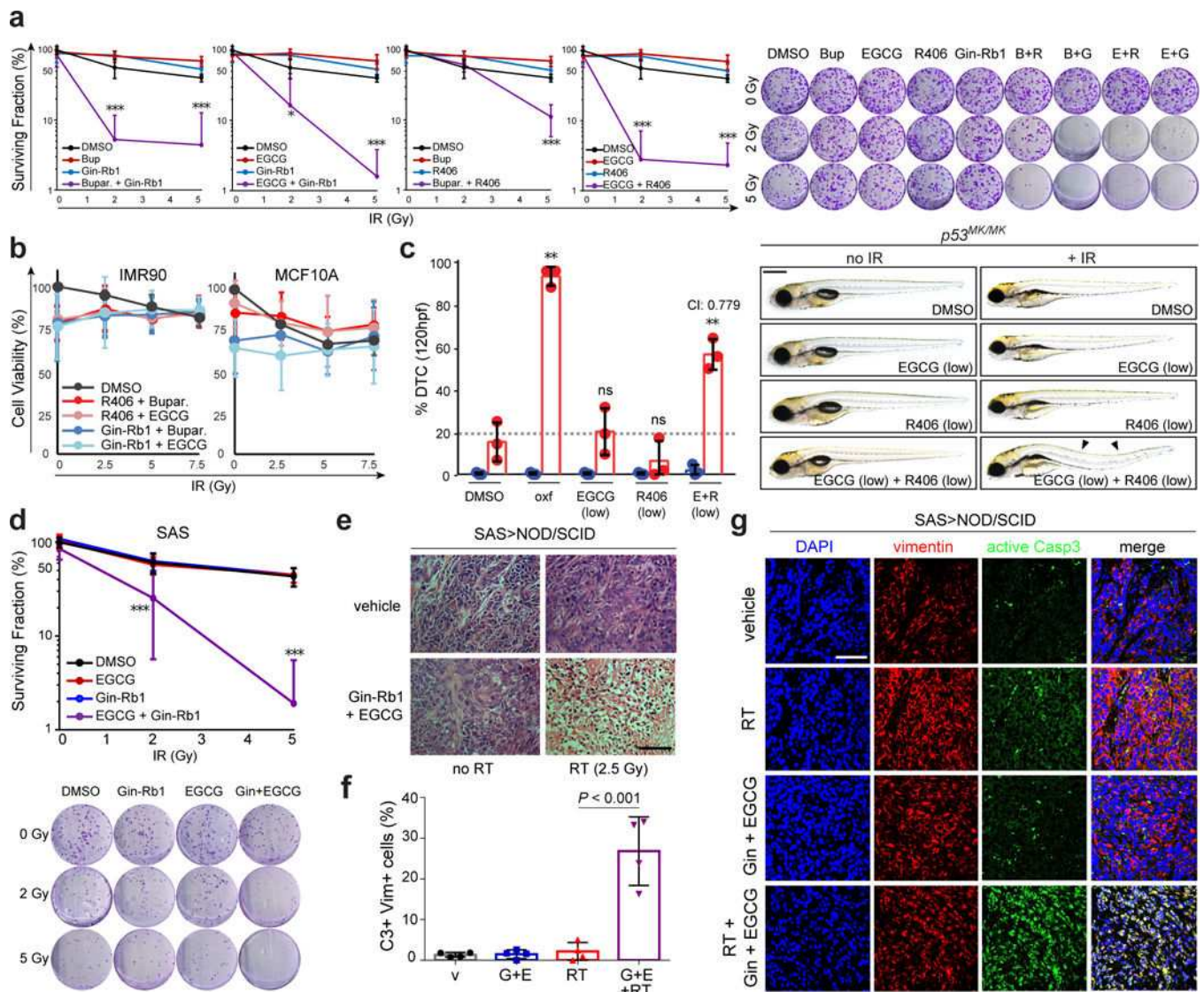


Fig. 7. Low-dose IRAK1 and PIN1 inhibitors synergistically suppress R-RT *in vitro* and *in vivo*. (a-b) HeLa (a) and non-tumorigenic IMR90 and MCF10A cells (b) treated with indicated IRAK1 and PIN1 inhibitors at subtherapeutic doses (Buparvaquone: 0.5 $\mu\text{g}/\text{mL}$, R406 0.1 $\mu\text{g}/\text{mL}$, Ginsenoside Rb1 5 $\mu\text{g}/\text{mL}$, and EGCG 5 $\mu\text{g}/\text{mL}$; see Fig. 5a) and indicated γIR doses (Gy), and analyzed by clonogenic assay at 14 dpIR (a, with representative images to the right) or alamarBlue at 5 dpIR (b). Data represented as means \pm SD of $n = 3$ independent experiments (a, b left) and $n = 4$ independent experiments (b, right) performed in triplicates. (c) $p53^{\text{Mk/Mk}}$ embryos treated with subtherapeutic doses of EGCG (40 $\mu\text{g}/\text{mL}$) and R406 (20 $\mu\text{g}/\text{mL}$) and 0 or 15 Gy TBI at 18 hpf analyzed for DTCs at 120 hpf. Data represented as means \pm SD of $n = 3$ independent experiments, with representative images shown to the right. P value is relative to DMSO-treated irradiated embryos (bar 2). CI, combination index, see Supplementary Fig. 7f. Scale bar, 0.5 mm. (d) Surviving fractions of SAS cells treated with subtherapeutic doses of Gin-Rb1 (5 $\mu\text{g}/\text{mL}$) and/or EGCG (5 $\mu\text{g}/\text{mL}$) at indicated IR exposures (Gy), analyzed 14 dpIR. Representative images shown

below. Data represented as means \pm SD of $n = 3$ independent experiments performed in triplicates. **(e-g)** SAS (2×10^6 cells)-derived tumor xenografts grown in NOD/SCID mice with $n = 5$ animals per indicated group analyzed by haematoxylin and eosin (H&E) staining **(e)** and immunofluorescence confocal microscopy with indicated antibodies **(f-g)** 24 days post-implantation. See Methods for detailed implantation, RT, drug delivery and staining protocols. Scale bars, 100 μm **(e)** and 80 μm **(g)**. Data in **(f)** are from the analysis of $n = 4$ independent samples per group with 3 independent images (as in **(g)**) scored per tumor. α -Vimentin and α -active caspase-3 mark human and apoptotic cells, respectively. Unless otherwise indicated, data throughout are expressed as means \pm SD, * $P < 0.05$, ** $P < 0.005$, *** $P < 0.0005$, *ns*, not significant, two-tailed Student's *t*-test. See Supplementary Table 4 for statistics source data including precise *P* values.